Journal of Rock Mechanics and Geotechnical Engineering 17 (2025) 3479–3501

Contents lists available at ScienceDirect

Journal of Rock Mechanics and Geotechnical Engineering

journal homepage: www.jrmge.cn

Full Length Article

Dynamic failure modes of large-scale underground caverns with complex geological structures

Yingjie Xia [a, b, c], Bingchen Liu [a, b], Danchen Zhao [a, b, d, *], Chun'an Tang [a, b], Hai Yang [e], Jian Chen [e]

[a] State Key Laboratory of Coastal and Offshore Engineering, Dalian University of Technology, Dalian, 116024, China
[b] School of Civil Engineering, Dalian University of Technology, Dalian, 116024, China
[c] State Key Laboratory of Geomechanics and Geotechnical Engineering Safety, Institute of Rock and Soil Mechanics, Chinese Academy of Sciences, Wuhan, 430071, China
[d] Department of Civil and Environmental Engineering, The Hong Kong Polytechnic University, Hung Hom, Kowloon, Hong Kong, China
[e] CNPC Chuanqing Drilling Engineering Company Limited, Chengdu, 610051, China

ARTICLE INFO

Article history:
Received 14 April 2024
Received in revised form
27 November 2024
Accepted 4 December 2024
Available online 1 March 2025

Keywords:
Columnar jointed rock mass (CJRM)
Underground caverns
Interlayer shear weakness zone (ISWZ)
Numerical simulation
Dynamic response

ABSTRACT

Rock masses are often exposed to dynamic loads such as earthquakes and mechanical disturbances in practical engineering scenarios. The existence of underground caverns and weak geological structures like columnar jointed rock masses (CJRMs) and interlayer shear weakness zones (ISWZs) with inferior mechanical properties, significantly undermines the overall structural stability. To tackle the dynamic loading issues in the process of constructing subterranean caverns, a programmable modeling approach was utilized to reconstruct a large-scale underground cavern model incorporating ISWZs and columnar joints (CJs). By conducting dynamic simulations with varying load orientations, the analyses focused on the failure patterns, deformation characteristics, and acoustic emission activity within the caverns. Results revealed that the failure modes of the underground caverns under dynamic loading were predominantly tensile failures. Under *X*-direction loading, the failed elements were mainly distributed parallel to the CJs, while under *Y*-direction loading, they were distributed parallel to the transverse weak structural planes. Furthermore, the dynamic stability of the overall structure varied with the number of caverns. The dual-cavern model demonstrated the highest stability under *X*-direction loading, while the single-cavern model was the least stable. Under *Y*-direction loading, the cavern stability increased with the number of caverns. Importantly, different weak structures affected the dynamic response of caverns in different ways; the CJRMs were the primary contributors to structural failure, while ISWZs could mitigate the rock mass failure induced by CJs. The findings could offer valuable insights for the dynamic stability analysis of caverns containing CJRMs and ISWZs.

1. Introduction

Columnar jointed rock masses (CJRMs) are characterized by a multitude of inherent tensile fracture structures. This results in marked anisotropic mechanical properties within these rock formations (Jiang et al., 2014; Hatzor et al., 2015; Jin et al., 2015; Meng et al., 2019; Xia et al., 2020a). In China, these rock masses have been encountered during the construction of major hydropower stations, including Tongjiezi, Xiluodu, and Baihetan. The unique mechanical responses and failure modes of CJRM during excavation and blasting are vital for the stability analysis of these engineering projects (Ishida et al., 2014; Xia et al., 2022; Zhao et al., 2022a). This significantly influenced the subsequent construction phases of the Baihetan project. Additionally, another geologically weak structure, known as the interlayer shear weakness zones (ISWZs), was identified during the construction process. These zones also have a significant impact on the stability of the surrounding rock (Xu et al., 2012, 2015). Furthermore, the dynamic stability analysis of rock

* Corresponding author. State Key Laboratory of Coastal and Offshore Engineering, Dalian University of Technology, Dalian, 116024, China.
E-mail address: danchen-simon.zhao@connect.polyu.hk (D. Zhao).
Peer review under responsibility of Institute of Rock and Soil Mechanics, Chinese Academy of Sciences.

https://doi.org/10.1016/j.jrmge.2024.12.017

engineering projects becomes increasingly complex due to stress redistribution caused by mechanical disturbances, explosive excavation, seismic events, and the interactions between CJRMs and ISWZs. This complexity presents significant challenges for the safety and stability control of structures in fields of water resources, hydropower, and mining tunnels (Feng et al., 2016,2017; Jiang et al., 2019). Therefore, investigating the dynamic failure modes and stability in large-scale underground caverns that incorporate multiple weak structures is crucial for the construction of related engineering projects. A comprehensive understanding of these complex interactions is essential for the design and implementation of safe and reliable engineering solutions under dynamic loading conditions.

The current research on CJRMs is primarily focused on understanding their formation mechanisms and mechanical properties (Bosshard et al., 2012; Phillips et al., 2013; Jin et al., 2015; Xia et al., 2022). Particularly, the analysis of mechanical characteristics is primarily focused on their relevance to engineering projects. The investigation into the mechanical attributes of CJRM is effectively conducted through in situ tests, laboratory experiments, and numerical simulations (Jiang et al., 2014; Ji et al., 2017; Mu et al., 2019). In situ tests and observations are crucial for investigating the mechanical properties of rock masses. For instance, at the Baihetan Hydropower Station, researchers have thoroughly examined the fundamental mechanical properties and failure modes of CJRMs under static loading through rigid plate bearing tests, central hole deformation tests, and P-wave testing (Shan and Di, 2013; Fan et al., 2018; Xia et al., 2020a). However, in situ tests often require significant resources and time, and the data obtained can be highly discrete (Ma et al., 2021, 2024). Laboratory experiments, on the other hand, effectively address these issues and have been widely applied in the study of CJRMs. The studies have brought to light the unique patterns of mechanical behavior and failure characteristics in different structural components of CJRMs, including basalt columns and columnar joints (CJs) (Jiang et al., 2020a, 2020b; Xia et al., 2020b, 2020c). The results indicate that CJRMs exhibit anisotropic characteristics and size effects in terms of compressive strength and elastic modulus. However, laboratory experiments are often limited by testing technology and scale, making large-sized rock mass experiments particularly challenging. Numerical simulations offer an economical, convenient, and efficient method that can simulate actual engineering conditions and construct complex structures. Simulation methods such as the discrete element method (DEM), three-dimensional distinct element code (3DEC), and Rock Failure Process Analysis System (RFPA) have been used to study the mechanical properties and failure modes of CJRMs (Jin et al., 2015; Liu et al., 2022; Zhao et al., 2022b, 2023). The numerical results are highly consistent with experimental outcomes. Under dynamic loading, the Split Hopkinson Pressure Bar (SHPB) system is widely employed in laboratory experiments to analyze the dynamic mechanical response of rocks (Dai et al., 2010; Wu et al., 2016). This differs from the electro-hydraulic servo universal testing machine loading under static loading. Physical experiments have shown that rocks primarily undergo tensile failure under dynamic loading, diverging from the tensile, shear, and sliding failures observed under static loading. Since rock dynamic mechanics are based on stress wave theory, researchers have focused their studies on the propagation patterns of stress waves to understand the interaction between stress waves and joint fractures (Huang, 2011; Wang et al., 2020), such as the joint roughness and inclination (Li et al., 2011; Huang et al., 2022). Significant progress has also been made in the dynamic constitutive models of jointed rock masses, such as the dynamic damage constitutive model and the equivalent continuum model (Ning et al., 2003; Li and Ma, 2009; Liu et al., 2015). Numerical methods have been extensively applied to investigate the dynamic mechanical properties of rocks, with improved discontinuous deformation analysis (DDA), FLAC3D, and RFPA methods (Yilmaz, 2013; Liao et al., 2016; Zhang et al., 2018; Xia et al., 2023). These studies have provided systematic insights into the dynamic mechanical properties and failure modes of jointed rock masses, laying a solid foundation for further research and practical applications in the field of geotechnical engineering.

The engineering stability analysis of CJRMs, beyond the acquisition of fundamental mechanical parameters and the analysis of failure modes, is of critical importance. In actual engineering scenarios, CJRMs often coexist with other geological structures, and construction processes such as blasting and disturbances can significantly impact the stability of engineering projects. This has led to a surge in scholarly interest in this area, with numerous researchers conducting extensive and in-depth studies. A large number of scholars have comprehensively explored the development and evolution laws of surrounding rock failure during and after excavation through field observations, model tests, and numerical simulations (Kwon et al., 2009; Jiang et al., 2017, 2020c; Cai et al., 2023; Guo et al., 2023). At the same time, the factors affecting the stability of surrounding rock were further studied, such as support pressure, the number of excavated blocks, joint direction, and weak geological structures (Bhasin and Hoeg, 1998; Zhu et al., 2008; Ahmed and Iskander, 2012; Wang and Huang, 2014; Zhao et al., 2022a; Liu et al. 2024a, 2024b). However, processes such as blasting, excavation, and earthquakes represent a dynamic transition from transient stress release to eventual static stress (Li et al., 2014; Zhu et al., 2014). Dynamic disturbances like earthquakes and blasting can induce numerous micro-fractures in rock engineering, leading to the deformation and failure of underground structures, thereby affecting the dynamic stability of underground structures. Li et al. successfully evaluated the stability of caverns and structural displacement by integrating microseismic monitoring with a continuous medium model (Li et al., 2020, 2021). Sun et al. and Tang et al. investigated the dynamic response characteristics of double parallel and double-arch tunnels through shaking table tests (Sun et al., 2011; Tang et al., 2023). Ömer Aydan et al. summarized various shaking table model test results and proposed empirical formulas for seismic stability, which proved to be effective (Aydan et al., 2010). However, these methods are limited by geological structures, testing technologies, and scale effects. Therefore, establishing numerical models that can accurately reflect complex geological and stress conditions, as well as the dynamic response and failure evolution, is a vital tool for analyzing the dynamic stability of underground structures. Manouchehrian and Cai (2018) concluded through numerical analysis that the presence of faults is a primary influencing factor for tunnel rock bursts. Fu et al. and Deng et al. noted that joints exhibit a damping effect on stress waves and that the orientation of joints affects structural damage, demonstrating the significant impact of the structure on its dynamic response (Deng et al., 2014, 2015; Fu et al., 2017). Zhu et al. (2010) simulated the mechanical response and failure processes of underground caverns under dynamic disturbances using the RFPA method, indicating that the instability of caverns increases with the intensity and duration of dynamic disturbances. Cui et al. (2016) investigated the impact of C2 ISWZs on seismic stability, highlighting their significant influence on cavern stability, with most of the deformation being generated by them.

A significant portion of existing research has focused on the deformation and failure characteristics of underground structures post-excavation under static conditions, as well as the dynamic response of these structures under dynamic disturbances. These studies, however, predominantly concentrate on single geological structures, which inadequately address the complexity of on-site

engineering scenarios. Zhao et al. (2022a) have significantly contributed to the understanding of the stability and failure mechanisms in underground caverns with intricate structures. However, their work is limited to static analysis and does not cover the dynamic loading stability of large-scale CJRMs. Furthermore, in simulation studies on CJRMs, the cross-sections of CJs are often represented as regular quadrilaterals, pentagons, or hexagons, which do not accurately reflect the actual structure of CJRMs.

This study aims to address the existing gaps in research by utilizing numerical simulations to assess how dynamic stresses affect the stability of large-scale CJRMs and ISWZs in the rock mass. Initially, 3D numerical models with varying numbers of caverns were constructed using digital image processing techniques, based on the geological data from the left bank of the Baihetan Hydropower Station. These models were then subjected to dynamic loading to investigate the dynamic response of large-scale underground cavern structures under different loading directions. Furthermore, the study identified failure traits in caverns with different chamber counts and assessed the dynamic stability effects of large CJRMs and ISWZs on rock masses. The findings from this research are expected to provide valuable insights for the dynamic stability analysis of underground caverns containing weak structures such as large-scale CJRMs and ISWZs.

2. Engineering geological analysis

2.1. Engineering background

The Baihetan Hydropower Station, situated within the jurisdictions of Ningnan County in Sichuan Province and Qiaojia County in Yunnan Province, represents the second tier of the cascade development on the lower reaches of the Jinsha River. Positioned approximately 182 km upstream from the Wudongde Dam and 195 km downstream from the Xiluodu Hydropower Station, the station maintains a normal reservoir level at 825.0 m above sea level, boasting a total reservoir capacity of 2.063×10^{11} m^3. The facility is equipped with eight 1,000,000 kW (1 GW) hydroturbine generator units on both the left and right banks, amassing a colossal installed generation capacity of 16,000,000 kW (16 GW). This establishment stands as a global leader in terms of the largest unit capacity for hydroturbine generator sets.

2.2. Engineering geological condition

The left bank surge cavern of the Baihetan Hydropower Station is located in a high mountain gorge, characterized by complex geological conditions, as illustrated in Fig. 1, which shows the left bank geology. The left bank features an extensive distribution of columnar jointed basalt, faults, interlayer shear zones, and randomly developed fractures. The basaltic rock formations on the left bank are composed of 11 distinct layers, predominantly featuring lava and brecciated lava from the top downwards. These layers are predominantly diorite, and aphanitic, with minor amounts of microcrystalline and vesicular basalt, and columnar joints are observed in the aphanitic basalt (Fig. 2). The four surge chambers are situated between the $P_2\beta_2^2 - P_2\beta_3^3$ strata. Additionally, the C2 ISWZ traverses through them. The CJs are predominantly developed in the $P_2\beta_3$ layer, with the columns varying in size and length.

Fan et al. (2018) conducted a study on the dimensional characteristics of basalt columns through field observations, categorizing them into three types based on distinct features: (1) The first type of columnar jointed basalt is characterized by fully developed internal columnar joints with intact columnar structures. These columns have diameters ranging from approximately 13-25 cm, mainly distributed in the $P_2\beta_3^3$ layer. (2) The second type of columnar jointed basalt differs in that its columnar structures have larger diameters, ranging from 25 to 40 cm, primarily developed in the $P_2\beta_3^2$ layer. (3) The third type of columnar jointed basalt exhibits irregular development of internal columnar joints, with diameters ranging from about 0.5 to 2.5 m. These joints do not cut the basalt into complete columnar structures. The C2 interlayer slip zone is exposed at the top and middle parts of the four surge caverns, with a width ranging from 5 to 60 cm. The rock masses on either side of the slip zone are highly fractured, predominantly displaying a shattered structure, with some areas exhibiting a disintegrated structure.

2.3. Geostress distribution

The initial geostress in the Baihetan left bank slope, with horizontal depths between 30 and 200 m and vertical burial depths of 40–280 m, is depicted in Fig. 3 (Shi et al., 2020). The first principal stress magnitudes on the left bank vary from 5.0 MPa to 12.4 MPa, trending SSE 129°–184° with an average dip of 23°. The second principal stress, ranging from 7.0 MPa to 9.0 MPa, is directed N15°W and has an average dip angle of 48°. The third principal stress, with magnitudes of 3.5–6.0 MPa, is oriented NEE, featuring moderate dip angles and an average direction of N74°E. The ground stress is relatively low, with concentrations in and around the valley. The maximum horizontal principal stress trends between NWW and EW, intersecting the valley at angles of 60°–80°.

The Ningnan-Qiaojia county region is classified as a moderately seismic-prone area with a low historical level of seismic activity. Historically, the seismic magnitude in the Baihetan Hydropower Station dam area has not exceeded 6 on the Richter scale. According to the "Seismic Ground Motion Parameters Zonation Map of China" (GB 18306–2015, 2015), the peak ground acceleration for the Baihetan project area is 0.20*g*, and the characteristic period of the ground motion acceleration response spectrum is 0.45 s.

3. Numerical simulations

3.1. Constitutive relationships

The dynamic mechanical behavior of rock masses is a complex and 3D issue that requires consideration of the intricate structure of the rock and an investigation into the dynamic failure process and crack propagation. Therefore, simulating the dynamic mechanical behavior of rock necessitates meeting the following requirements: (1) accurately representing the complex structure of natural rock masses and (2) capturing the entire process of dynamic failure, particularly the initiation and propagation of cracks. The program developed by Tang et al. (2015, 2020) effectively addresses this challenge. Hence, the present study employs the finite element method (FEM), incorporating the Weibull statistical approach and the equivalent continuous damage mechanics method, to investigate the damage evolution process of underground cavern structures under dynamic loading.

In this paper, the constitutive relationship of elastic damage mechanics is used to describe the meso-mechanical properties of rocks, as shown in Fig. 4 (Li et al., 2017). Where f_c and f_t represent the uniaxial compressive and tensile strength of the unit. f_{cr} and f_{tr} represent the residual strength of the unit after phase transformation, separately. In addition, to truly reflect the progressive failure process of rock materials, Weibull distribution is used to describe the uneven material properties of rocks (Weibull, 1951):

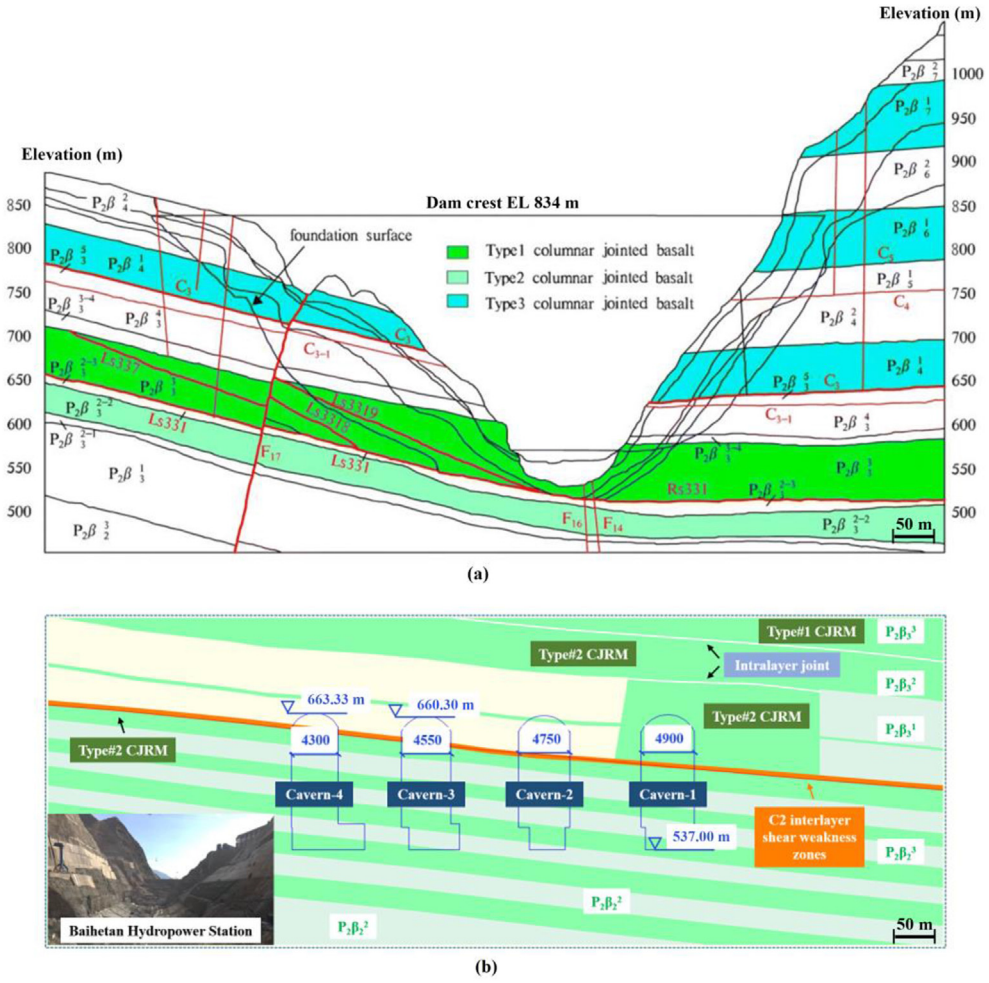

Fig. 1. The geological structure diagram of the left bank of Baihetan Hydropower Station (Shi et al., 2020).

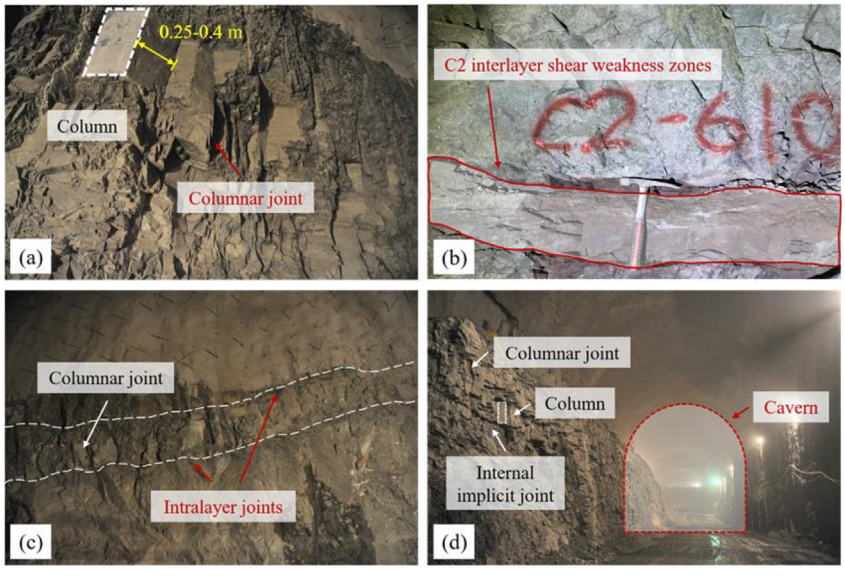

Fig. 2. Different geological structures in the left bank of Baihetan Hydropower Station: (a) Columnar joint; (b) Interlayer shear weakness zone; (c) Interlayer joint; and (d) Cavern (Zhao et al., 2022a).

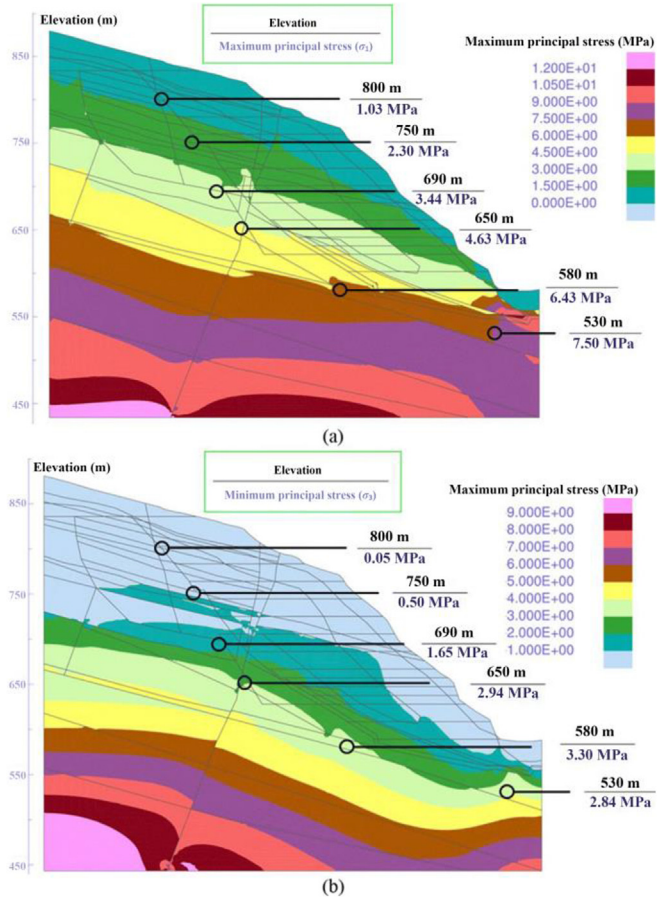

Fig. 3. Initial ground stress distribution on the left bank of Baihetan Hydropower Station: (a) Maximum principal stress; and (b) Minimum principal stress (Shi et al., 2020).

$$\varphi(\alpha)=\frac{m}{\alpha_0}\cdot\left(\frac{a}{\alpha_0}\right)^{m-1}e^{-\left(\frac{a}{\alpha_0}\right)^m} \tag{1}$$

where α is the mechanical parameter of the element, including compressive strength and elastic modulus; α_0 is the scale factor of the average mechanical parameter of the unit; m represents the uniformity of rock materials, which is related to the shape of material distribution. When the value of m is larger, the rock materials show obvious homogeneity. While the value of m is smaller, the rock materials show heterogeneity.

In this method, the element is assumed to be elastic at the initial stage, and its material elasticity depends on the Young's modulus and Poisson's ratio. When the stress on the element does not reach its strength, we consider the element to be elastic and then weaken its properties. In elastic damage mechanics, the elastic modulus of an element decreases with the progression of damage and is expressed as follows:

$$E=(1-D)E_0 \tag{2}$$

where D is the damage variable; and E and E_0 indicate the elastic moduli of the material at the current and initial stages, respectively.

The damage variable is measured by strain. When the meso-element is in the uniaxial tensile state (like the compressive state and the tensile state), in the initial stage, no damage occurs inside the element, and its stress-strain curve is linear-elastic, at which time $D=0$. However, when the strain reaches the elastic tensile strain threshold, the element is damaged, and the current damage variable is calculated as follows:

$$D=\begin{cases}0\ (\varepsilon\le\varepsilon_{t0})\\ 1-\dfrac{\lambda\varepsilon_{t0}}{\varepsilon}\ (\varepsilon_{t0}\le\varepsilon\le\varepsilon_{tu})\\ 1\ (\varepsilon\ge\varepsilon_{tu})\end{cases} \tag{3}$$

where λ is the element residual strength coefficient; $\varepsilon,\varepsilon_{t0},\varepsilon_{tu}$ are the equivalent strain, elastic tensile strain, and ultimate tensile strain, respectively. When the tensile strain exceeds the ultimate tensile strain, the meso-element completely fails. The ultimate tensile strain is calculated as Eq. (4), where η is the ultimate strain coefficient.

$$\varepsilon_{tu}=\eta\varepsilon_{t0} \tag{4}$$

In addition, the constitutive relation in the uniaxial state can be extended to the 3D stress state. In the multi-axial stress state, tensile strain ε is usually replaced by equivalent strain $\overline{\varepsilon}$ as shown in Eq. (5). When the equivalent strain reaches the strain limit, tensile failure occurs.

$$\overline{\varepsilon}=-\sqrt{\langle-\varepsilon_1\rangle^2+\langle-\varepsilon_2\rangle^2+\langle-\varepsilon_3\rangle^2} \tag{5}$$

where $\varepsilon_1,\varepsilon_2,\varepsilon_3$ are the three principal strains of the unit, and the calculation method of is $\langle\ \rangle$ shown as

$$\langle x\rangle=\begin{cases}x,\ x\ge0\\ 0,\ x<0\end{cases} \tag{6}$$

The failure of mesoscopic elements is defined by the Mohr-Coulomb criterion. When the element stress satisfies Eq. (7), it is considered that the element has compression/shear failure, and the damage parameters of the element are shown in Eq. (8).

$$\frac{1+\sin\varphi}{1-\sin\varphi}\sigma_1-\sigma_3\ge\sigma_c \tag{7}$$

$$D=\begin{cases}0 & (\varepsilon<\varepsilon_c)\\ 1-\dfrac{\lambda\varepsilon_c}{\varepsilon} & (\varepsilon\ge\varepsilon_c)\end{cases} \tag{8}$$

where σ_1 is the maximum principal stress, σ_3 is the minimum principal stress, σ_c is the uniaxial compressive strength of the unit, φ is the internal friction angle, and ε_c is the compressive strain.

In the process of dynamic finite element calculation, the space is discretized according to the Hamilton variational principle, and the dynamic equation is obtained by

$$M\ddot{u}+C\dot{u}+Ku=Q \tag{9}$$

where $\ddot{u}$, $\dot{u}$, u are the displacement, velocity and acceleration, respectively; and M, C, K are the mass, damping and stiffness matrices of the system, respectively. By using the Newmark method, the relation between velocity $\dot{\alpha}_{t+\Delta t}$ and displacement $\alpha_{t+\Delta t}$ at different time is introduced, and the differential equation is obtained by

$$\widehat{K}\alpha_{t+\Delta t}=\widehat{Q}_{t+\Delta t} \tag{11}$$

Among,

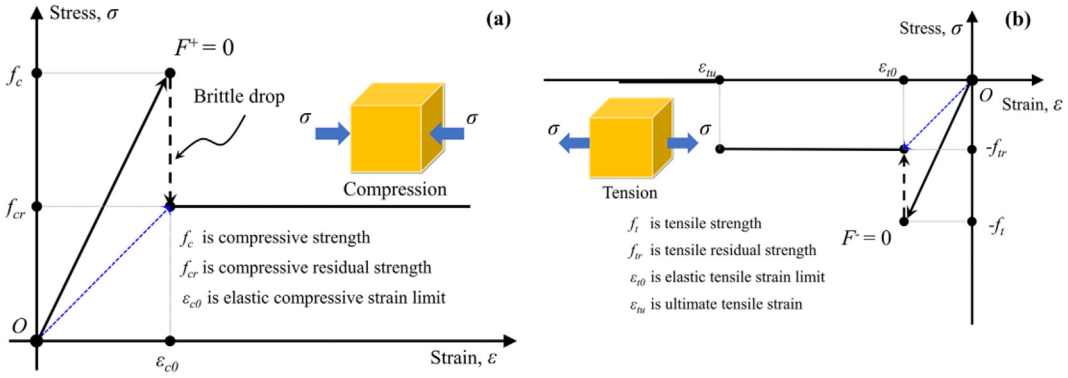

Fig. 4. Constitutive relation of elastic damage of rock under uniaxial stress: (a) Uniaxial compression; and (b) Uniaxial tensile (Li et al., 2017).

$$\widehat{K}=K+\frac{1}{\beta\Delta t^2}M+\frac{\gamma}{\beta\Delta t}C \tag{12}$$

$$\widehat{Q}=Q_{t+\Delta t}+M\left[\frac{1}{\beta\Delta t^2}(\alpha_{t+\Delta t}-\alpha_t)-\frac{1}{\beta\Delta t}\dot{\alpha}_t-\left(\frac{1}{2\beta}-1\right)\ddot{\alpha}_t\right]+C\left[\frac{\gamma}{\beta\Delta t}(\alpha_{t+\Delta t}-\alpha_t)+\left(1-\frac{\gamma}{\beta}\right)\dot{\alpha}_t+\left(1-\frac{\gamma}{2\beta}\right)\Delta t\ddot{\alpha}_t\right] \tag{13}$$

where β and γ are the integral coefficients of the Newmark method, when $\gamma \geq 0.5$, $\beta \geq 0.25(\gamma+0.5)^2$, the Newmark method is unconditionally stable.

3.2. Model establishment

To investigate the dynamic collapse patterns, deformation traits, stress allocation, and acoustic emission (AE) attributes of intricate, large-scale subterranean cavities. For this purpose, models featuring either one or two caverns were developed. The model development, as depicted in Fig. 5, is a four-stage process: (1) A stratified rock mass model was created with 3D modeling tools. It includes the C2 ISWZ and is based on geological data from the left bank of the Baihetan Hydropower Station; (2) The multi-scale CJs were generated using the Voronoi diagram technique; (3) Suitable locations within the layered rock mass were designated for the formation of corresponding large-scale CJRMs; and (4) The process of excavating the underground caverns was emulated. After completing the 3D digital model, it was divided into several layers. Then, the model was moved to numerical analysis software. As a result, the 3D numerical reconstruction model closely matches the geological conditions on the left bank of the Baihetan Hydropower Station. This ensures the model's accuracy and authenticity. In the realm of numerical simulations, the element count greatly influences both the accuracy of computation and the time required. While a greater number of elements can yield a more nuanced depiction of crack propagation, it also prolongs the computation time. Hence, drawing on extensive pilot calculations from prior research, this study struck a balance between computation time and precision. The final model comprises a total of 5,600,000 elements.

3.3. Parameter calibration

The characteristics of CJs and ISWZs are marked by their inferior mechanical properties and discontinuity. They are the primary sources of instability during the excavation of underground caverns, affecting their design, construction, and safety evaluations. It is crucial to analyze the dynamic mechanical reactions and failure patterns of these weak formations. Distinct features must be examined for different structures, such as the uniaxial compressive of basalts and the shear of CJs and ISWZs. In this model, the structures that necessitate calibration of mechanical parameters include the rock mass, CJs, and the C2 ISWZs. Geological field investigations were initiated, involving core drilling and sampling to procure experimental specimens. The specimens, with a diameter of 50 mm and a height of 100 mm, adhered to the standards set by the International Society for Rock Mechanics and Rock Engineering (ISRM) (Aydin, 2009). Following this, uniaxial compression tests were conducted on columnar basalt specimens, complemented by numerical tests under identical loading conditions, allowing for a comparison of yield stress-strain curves and failure modes. For CJs and the C2 ISWZs, direct mechanical testing to obtain relevant parameters is challenging. Instead, these parameters were inferred through indirect method and numerical experiments were performed to derive their shear stress-shear displacement curves and stress distribution profiles. Ultimately, the structural parameters within the numerical model were fine-tuned to align with the stress-strain curves and shear stress-displacement curves obtained from the laboratory tests. The calibrated mechanical parameters from the numerical simulation are presented in Table 1.

3.4. Numerical simulation loading scheme

During the construction of the Baihetan Hydropower Station, dynamic loadings such as cavern blasting excavation, human-induced disturbances, and seismic events trigger stress redistribution, complicating the stress conditions within the underground caverns. The dynamic stability of these caverns is critically important. To simulate the dynamic stability of different cavern configurations, this study considers three scenarios: no caverns, single caverns, and double caverns, as illustrated in Fig. 6a–c. Stress field analysis of the Baihetan Hydropower Station under seismic action, conducted by Yang et al. (2012) using FLAC3D, revealed the principal stress fluctuation range of 12.61–12.86 MPa. Furthermore, for effectively guiding the dynamic stability analysis of similar projects, the peak dynamic load was chosen to exceed the peak principal stress of the Baihetan Hydropower Station. Incorporating the dynamic mechanical research on CJRMs by Xia et al. (2023), a peak stress value of 14 MPa was ultimately chosen for the dynamic loading, applied as a triangular wave with reflective boundaries, as shown in Fig. 6d. The rise and fall times of the stress wave were both set at 0.002 s, considering that the frequency of blasting-induced seismic waves ranges from 100 Hz to 500 Hz, with a selected frequency of 250 Hz (corresponding to 0.002 s) based on comprehensive analysis. Additionally, to explore the different

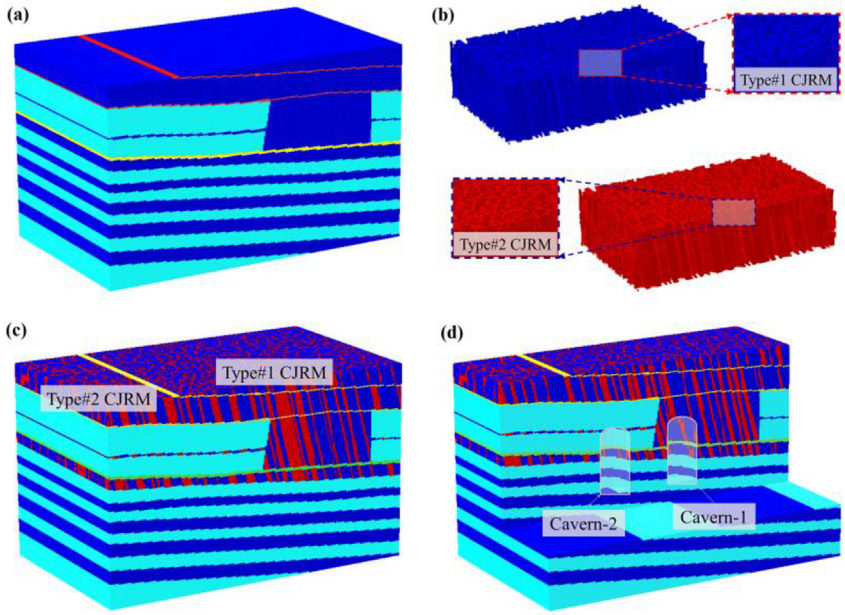

Fig. 5. Model building process: (a) Layered rock mass model (dark blue represents rock 2, light blue represents rock 1, red represents IJs, and yellow represents ISWZs), (b) CJ model, (c) CJRM model, and (d) Cavern excavation model (Zhao et al., 2022a).

impacts of S-wave and P-wave on the stability of underground caverns during seismic events, the triangular wave loading was applied in two directions, loading along the *X*-direction (simulating S-waves, Fig. 6e) and the *Y*-direction (simulating P-waves, Fig. 6f).

Considering the complex geological structure of the cavern's location, several cross-sections were established in the *X*-, *Y*-, and *Z*-directions to accurately analyze the failure modes and stress characteristics of different weak spots under dynamic actions. Fig. 7 illustrates the cross-sectional schemes, and their locations used for the numerical model analysis. Along the *X*-axis, cross-sections were set on both sides and in the middle of the two caverns, at positions of $X = 82$ m, 94 m, 106 m, 139 m, 151 m, and 164 m. On the *Y*-axis, cross-sections were established at the bottom and top of the caverns containing ISWZs, at positions of $Y = 55$ m, 56 m, 85 m, 87 m, 106 m, and 107 m. For the *Z*-axis, cross-sections were placed at the front, rear, and middle of the caverns, at positions of $Z = 63$m, 75.5 m, and 89 m.

4. Numerical results

4.1. Dynamic response of underground caverns

Generally, the dynamic failure of rock is processual. Under dynamic loadings, the stress propagates, reflects, and superposes within the rock mass, leading to stress redistribution. A part of the rock mass reaches critical strength and finally produces failure. The whole process of model failure, maximum principal stress, and acoustic emission under dynamic loads in different directions obtained by numerical simulation are shown in Figs. 8–11. It is observed from Fig. 8 that under the loading along the *X*-direction (compression wave), the stress propagation process can be divided into three stages: the first propagation stage (from the loading position to the right boundary of the model), the second propagation stage (reflection from the right boundary back to the loading position), and the cavern failure stage. Due to geological structural differences around the underground caverns at varying depths along the *X*-direction, a "delay" phenomenon is observed during stress propagation. After the second propagation stage, differences in principal stress distribution between the two caverns are apparent. Cavern-1, located in CJRMs with weaker strength, experiences tensile failure. The rock mass around it is subjected to compression, with a few areas showing concentrated compressive stress. In contrast, Cavern-2, situated in a more intact rock mass, exhibits no failure but is subjected to tensile stress induced by the tensile wave. During the cavern failure stage, cracks in Cavern-1 develop in the upper part along the direction of the CJs, while Cavern-2 shows only a few vertical cracks. The failure zone is primarily distributed at the interface between the ISWZ and the cavern, close to the loading direction, indicating tensile failure. Throughout the stress propagation process, the structures in the underground caverns predominantly experience tensile failure (indicated by blue units). This failure initiates and extends along the direction of stress propagation, with its distribution closely following the columnar joints. To further investigate stress

Table 1
Numerical simulation of mechanical parameters of different structures.

Structure	Elastic modulus (MPa)	Compressive strength (MPa)	Poisson's ratio	Gravity (10^{-5} N/mm^3)	Fraction angle (°)	C-T ratio
Rock1	40,000	400	0.25	2.65	30	5
Rock2	30,000	300	0.17	2.65	30	5
Intralayer joints	10,000	50	0.35	2.58	15	10
Columnar joints	8000	40	0.35	2.58	15	10
C2 interlayer shear weakness zones	12,000	60	0.35	2.73	30	10

Note: C-T ratio is the ratio of compression strength to tensile strength.

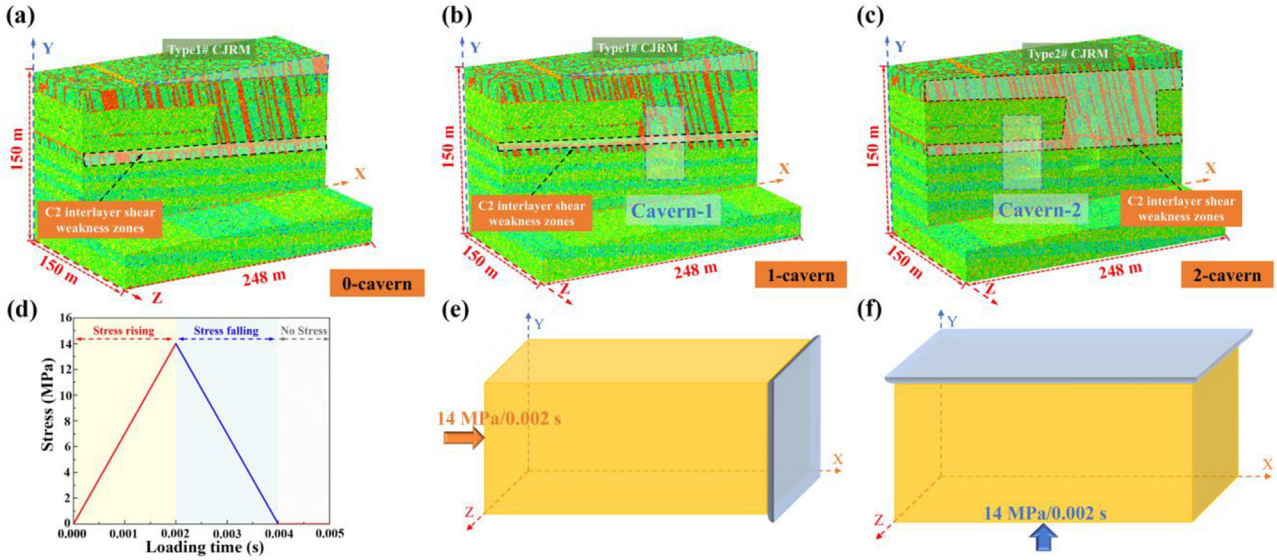

Fig. 6. The 3D reconstructed numerical model and dynamic loading schemes: (a) No cavern model; (b) Single cavern model; (c) Double cavern model; (d) Stress loading schemes; (e) Loading along the *X*-direction; and (f) Loading along the *Y*-direction.

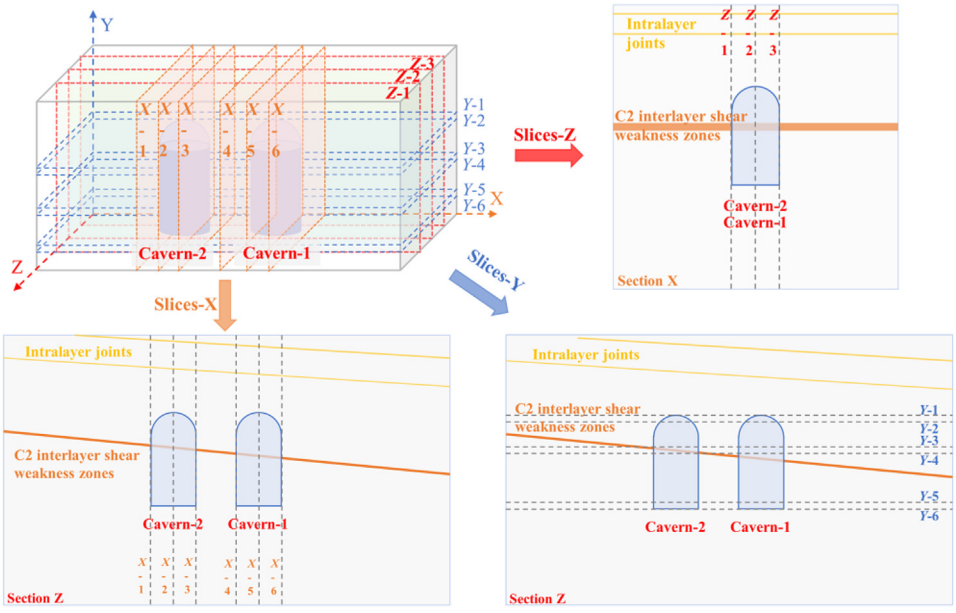

Slices	*X*-1	*X*-2	*X*-3	*X*-4	*X*-5	*X*-6	*Y*-1	*Y*-2	*Y*-3	*Y*-4	*Y*-5	*Y*-6	*Z*-1	*Z*-2	*Z*-3
Coordinate/m	82	94	106	139	151	164	107	106	87	85	56	55	89	73	65

Fig. 7. Profile schemes and location of the numerical model.

distribution characteristics in fragile structures, stress models along the *X*, *Y*-3, and *Z*-2 sections were analyzed at $t = 0.144$ s (after the second stress propagation).

The maximum principal stress cloud diagrams of each section are shown in Fig. 9. According to *Y*-3 and *Z*-2, tensile stress mainly distributes around the CJs, while the rock mass is primarily under compressive stress. The interlayer shear weakness zone, due to its weaker strength, exhibits multiple failures during loading, leading to a complex stress distribution. The top of Cavern-1 develops an obvious compressive stress concentration area, while the lower part produces minor tensile failure (*X*-5). The stress concentration area of tensile stress at the interface between the ISWZ and the left side of the cavern expands, matching the failure stage area. The *X* section of Cavern-2 shows a concentration area of compressive stress at the top of CJRM, and a clear boundary between the upper compressive area and lower tensile stress area is obvious. Thus, under dynamic loading along the *X*-direction, the overall failure of the underground cavern is tensile failure, parallel to the columnar joints. At the same time, the failure position starts at the interface between the ISWZ and the cavern.

Under the dynamic loading along the *Y*-direction, the dynamic response of the underground cavern differs from that under the *X*-

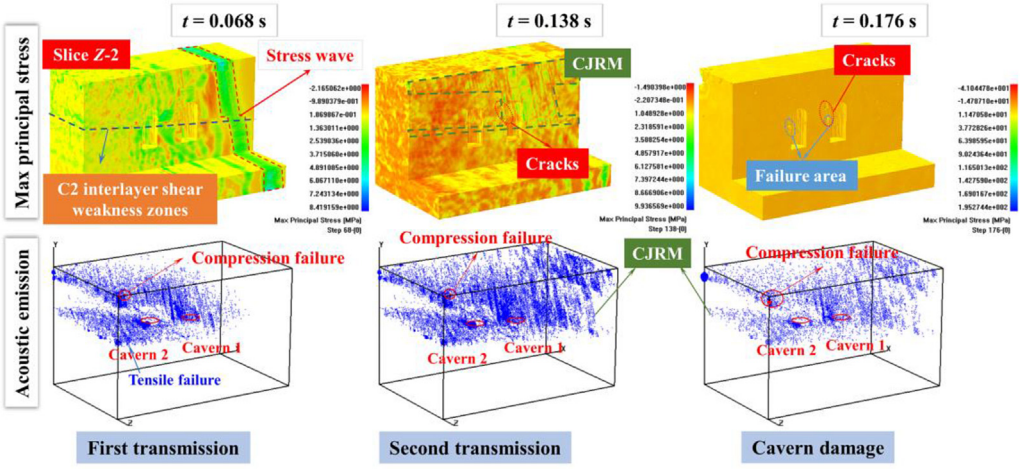

Fig. 8. The maximum principal stress and AE cloud diagram of the double cavern model under dynamic loading along the *X*-direction.

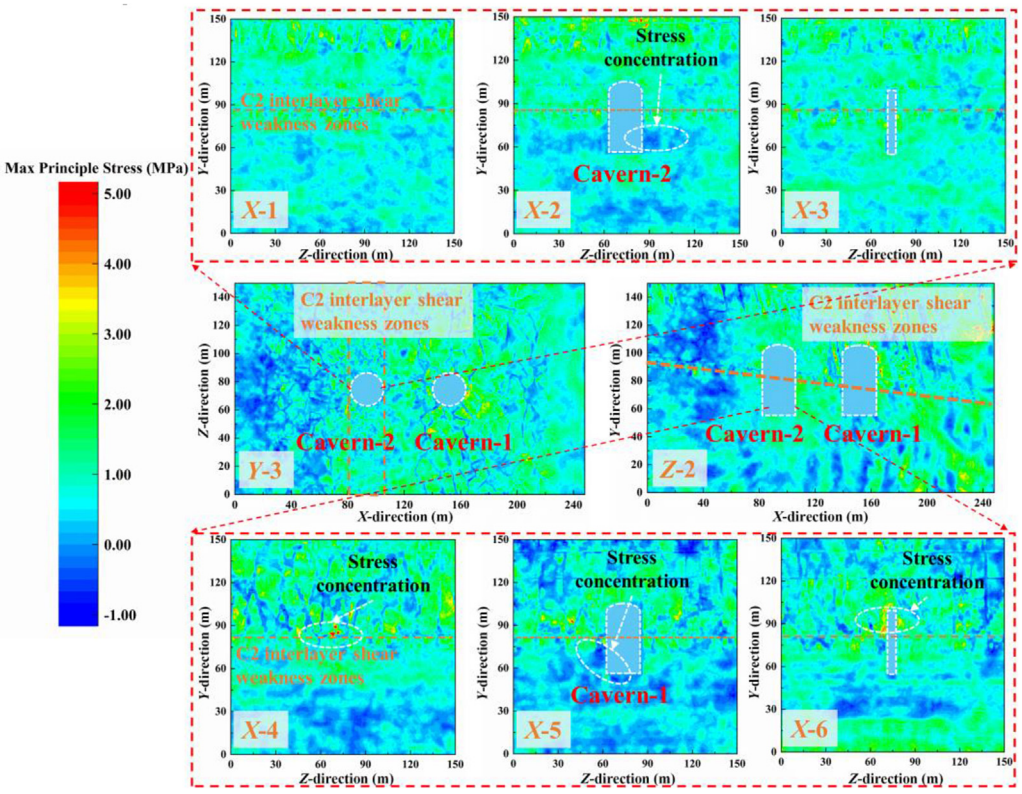

Fig. 9. Nephogram of the maximum principal stress in the model profile at $t = 0.144$ s under dynamic loading along the *X*-direction.

direction loading, as shown in Fig. 10. Initially, the stress propagation can be divided into four stages: the first propagation stage (from the loading position to the top boundary), the second propagation stage (from the top to the bottom), the third propagation stage (from the bottom to the top), and the cavern failure stage. Unlike the *X*-direction loading, the geological structure around the cavern remains uniform at the same depth in the *Y*-direction, resulting in the absence of a "delay" phenomenon in stress propagation. Cracks primarily develop at the interlayer joints and ISWZs. During the second stage, the number of failure elements along the interlayer joints gradually increases until cracks form. Failure occurs in the ISWZ, and cracks in the cavern distribute horizontally. However, no significant failure is observed in the CJRMs. After the third stage, the ISWZs and internal cracks in the cavern form through-cracks, with stress concentration areas appearing at the top of the interlayer joint. As stress continues to propagate, failure in the interlayer joints, ISWZs, and internal cracks within the cavern intensify. Ultimately, three transverse horizontal failure planes spanning the entire structure are formed during the failure stage. In addition, the cavern structure predominantly fails in tension, with failure distributed along the planes of the ISWZs and interlayer joints.

The time of $t = 0.124$ s (after the third stress propagation) is selected to analyze the six sections along the *X*-axis, *Y*-3, and *Z*-2

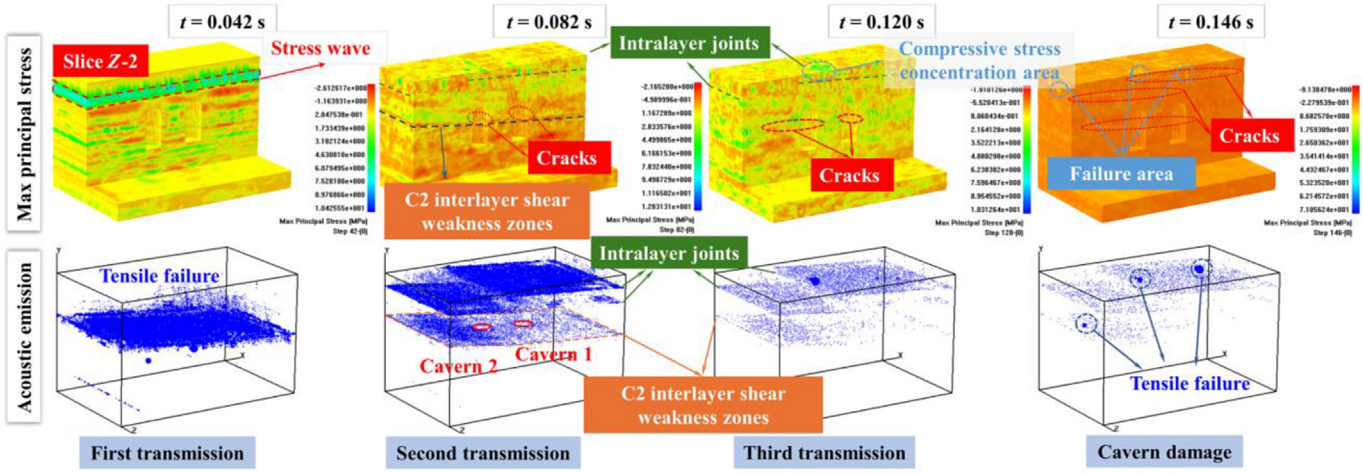

Fig. 10. The maximum principal stress and AE cloud diagram of the double cavern model under dynamic loading along the *Y*-direction.

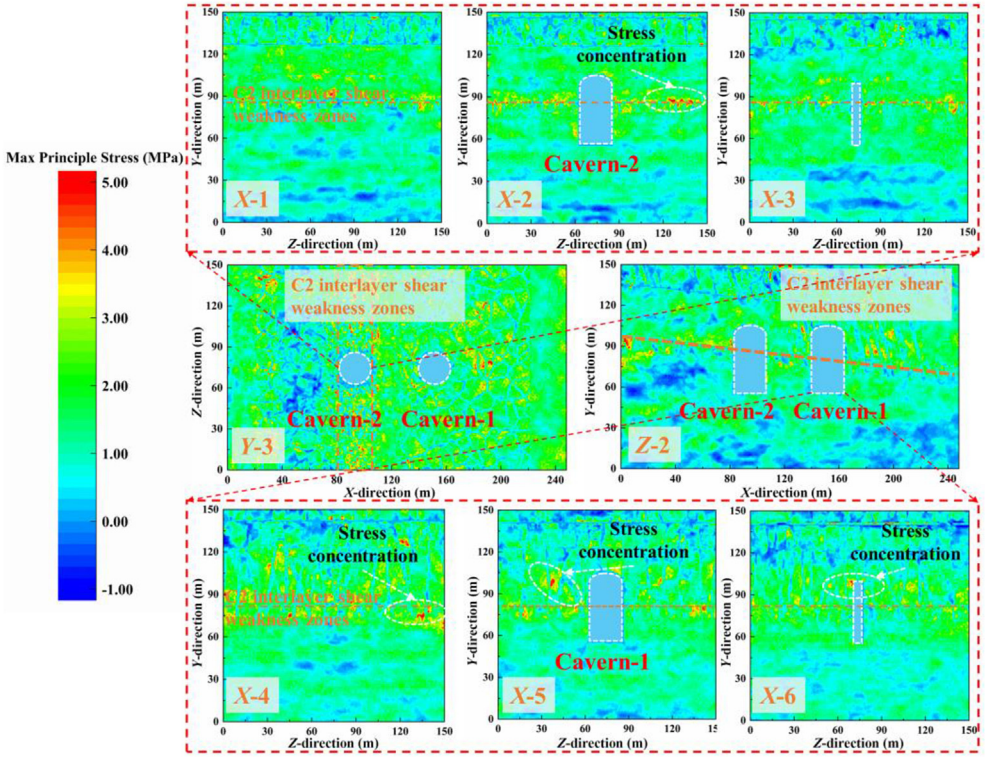

Fig. 11. Nephogram of the maximum principal stress in the model profile at $t = 0.124$ s under dynamic loading along the *Y*-direction.

sections. Their maximum principal stresses are shown in Fig. 11. Different from *X*-direction loading, there are a large number of compressive stress concentration areas in the ISWZ and the overall model distribution (*Y*-3). The tensile stress is significant at the interlayer joints, forming two diagonal tensile stress areas (*Z*-2). The compressive stress concentration area around Cavern-1 (*X* section) increases, mainly in the CJRMs. At the same time, tensile failures occur at the top and bottom boundaries of the cavern. Around Cavern-2 and the interface with the ISWZ, many failure areas appear, with stress values being negative (i.e. tensile stress) (*Y*-3). For the *X*section, the compressive stress concentration areas develop on both sides of the ISWZ. The tensile stress is concentrated in the ISWZ and the upper interlayer joints. Under *Y*-direction loading, the low tensile strength of the weak structure leads to the occurrence of tensile failure and finally forms a horizontal failure plane. Hence, although under dynamic loadings, both directions are a tensile failure, the model failure under *X*-direction loading is parallel to the CJRMs, whereas, under *Y*-direction loading, it is parallel to the horizontal weak structural planes. Moreover, the internal cracks within the caverns differ, and both are perpendicular to the loading direction. In contrast, the horizontal through cracks caused by *Y*-direction loading have a far greater impact on structural stability than the vertical through cracks caused by *X*-direction loading.

Figs. 12 and 13 show the stress-time and strain-time curves at the weak structures of each cavern under dynamic loading. Under

X-direction loading (Fig. 12), monitoring points at different positions within the cavern reach their stress peak values at different times. Complex structures (CJRMs) have a delayed peak stress time, such as at the top of Cavern-1 (Fig. 12a and c). Moreover, during the dynamic loading process, when the first stress peak reaches, the rock mass experiences the highest stress. Then the stress fluctuates continuously with overall minor stress differences. At the same time, the strain at all monitoring points does not exceed the strain limit. The strain peak at the top of Cavern-2, located at the CJRMs, is large (Fig. 12b). In Fig. 12e and f, monitoring points in the ISWZ exhibit strain accumulation, resulting in significant brittle failure. However, the stress does not reach the limit, indicating that rock failure at this location is controlled by strain. During construction, reinforcement and support should be applied. Under *Y*-direction loading, the change curves of stress and strain with time are as shown in Fig. 13. The stress values at the bottom and top center of the cavern are small. During the second and third stages of stress propagation, the peak values of stress and strain at each monitoring point gradually increase. At the failure stage, a sudden increase in strain occurs at the cavern's bottom center, but this does not cause failure. Additionally, the stress fluctuation at the position of the ISWZ is significant, and the strain accumulation phenomenon is obvious. Finally, brittle rock failure occurs and the strain drops to 0 suddenly. Thus, regardless of *X*- or *Y*-direction dynamic loading, the failure location occurs at the interface between the ISWZ and the cavern. The strain at the cavern's top and bottom center is higher in the failure stage, necessitating reinforcement in practical engineering.

Rock mass undergoes deformation and accumulates strain energy during loading, releasing a large amount of energy upon failure. Therefore, AE can also be used to assess rock instability and crack propagation. Fig. 14 shows the variation of AE count and energy with time under dynamic loading in different directions. Under *X*-direction loading (Fig. 14a), there are two obvious peaks in the AE count during the stress propagation period. The first peak corresponds to unit failure between the two caverns in the CJRM area. The second peak occurs at the time when extensive failure appears in the upper CJRMs stress. The failure is caused by the stress wave after reflecting off the right boundary. The AE energy is uniform and the accumulative energy does not increase significantly. At the cavern structure failure stage, the AE count gradually increases, and the accumulative energy shows a stepwise change. Additionally, the AE curve under *Y*-direction loading also contains two peaks (Fig. 14b), but the AE count far exceeds that under *X*-direction loading. The peaks in the AE count occur during the failure of the ISWZ and top interlayer joints. Overall, the peak phenomena are more apparent, and the increase in AE during the failure stage is more significant. However, the pattern of AE energy differs from that under *X*-direction loading. The energy surge phenomenon occurs during the propagation stage, caused by a dramatic increase in the AE count.

4.2. Dynamic response of different numbers of caverns

4.2.1. Dynamic loading along the X-direction

In geotechnical engineering, cavern excavation is typically performed in stages, rather than simultaneously, leading to stress redistribution throughout the entire structure after each stage. Therefore, it is crucial to investigate the dynamic response of varying numbers of caverns under dynamic loading. Using numerical simulation, the failure modes and maximum principal stress distributions for different cavern configurations in the *Z*-2 and *X* sections were analyzed, as shown in Fig. 15. As the number of caverns increases, the compressive stress around the caverns decreases, while the tensile stress exhibits more complex variations. For the case with no caverns, a few failure units are observed around the CJs, with localized areas of concentrated compressive stress in the rock mass. In the single cavern scenario, the failure units gradually converge, forming cracks parallel to the joints. Both vertical and horizontal cracks develop within the cavern, predominantly resulting from tensile failure. In the double cavern configuration, cracks propagate further, with horizontal cracks appearing inside Cavern-2. The internal stress in Cavern-2 is primarily tensile stress. Additionally, a small area of concentrated compressive stress is observed beneath the CJs in the ISWZ. In summary, an increase in the number of caverns significantly reduces compressive stress but intensifies failure in weak structures, particularly at ISWZs and CJs.

Fig. 16 shows the changes in horizontal stress and strain distribution at the weak structure in the cavern at different propagation stages. The area with significant changes in stress and strain at the top of the cavern is located at the CJRM (Fig. 16a and e). An increase in the number of caverns helps reduce the top stress, decreasing the fluctuation of horizontal stress and strain. Fig. 16b, c, f, and g show the horizontal stress and strain curves when the ISWZ passes through Cavern-2 and Cavern-1. For horizontal stress, an increase in the number of caverns can reduce stress fluctuation. However, due to the presence of the ISWZ, both exhibit obvious strain peaks and have reached failure. The cavern bottoms are located in the rock mass area, so there is not much difference in the distribution of horizontal stress and strain (Fig. 16d and h). The presence of caverns significantly reduces the peak values of stress and strain in the surrounding rock mass. However, high strain concentrations occur at the cavern boundaries, highlighting the need for timely reinforcement during construction.

Through the above analysis, it is evident that caverns have a significant impact on ISWZs. Therefore, focusing on the interface between the ISWZ and the cavern, the variation curves of stress and strain with loading time are plotted in Fig. 17. Throughout the whole dynamic loading process, the stress at the monitoring points never reaches the strength limit, and the rock mass undergoes brittle failure due to strain accumulation. The red monitoring points, located above and below the cavern, lie within the CJRMs and exhibit larger stress fluctuations. Vertically, an increase in the number of caverns reduces early-stage stress fluctuations before failure but causes a slight increase in stress during the failure stage. In terms of strain, the presence of caverns exerts a significant influence. During the early stage of loading, strain fluctuations are minimal or even absent. However, strain accumulates in the later stage, eventually leading to brittle failure of the rock mass. Therefore, although cavern excavation induces brittle failure at the ISWZ, it significantly reduces early-stage strain fluctuations during stress propagation.

Fig. 18 shows the variations curve of single-step AE count and accumulative energy with time under different direction loading. For the *X*-direction loading (Fig. 18a), the presence of caverns makes the surrounding rock mass in one free-face state. Therefore, models containing caverns have more AE counts and energy than complete models. Comparing single and double caverns, it is evident that the number of caverns can reduce failure and extend the failure time. Thus, an increase in the number of caverns can enhance the dynamic stability of the structure under certain conditions.

4.2.2. Dynamic loading along the Y-direction

Under *Y*-direction loading, the failure modes and maximum principal stress of the numerical model in the *Z*-2 and *X* sections are as shown in Fig. 19. Similar to *X*-direction loading, as the number of caverns increases, the structural compressive stress gradually decreases. The crack expansion increases forming cracks, and all are tensile failures. However, the cracks under *Y*-direction loading are

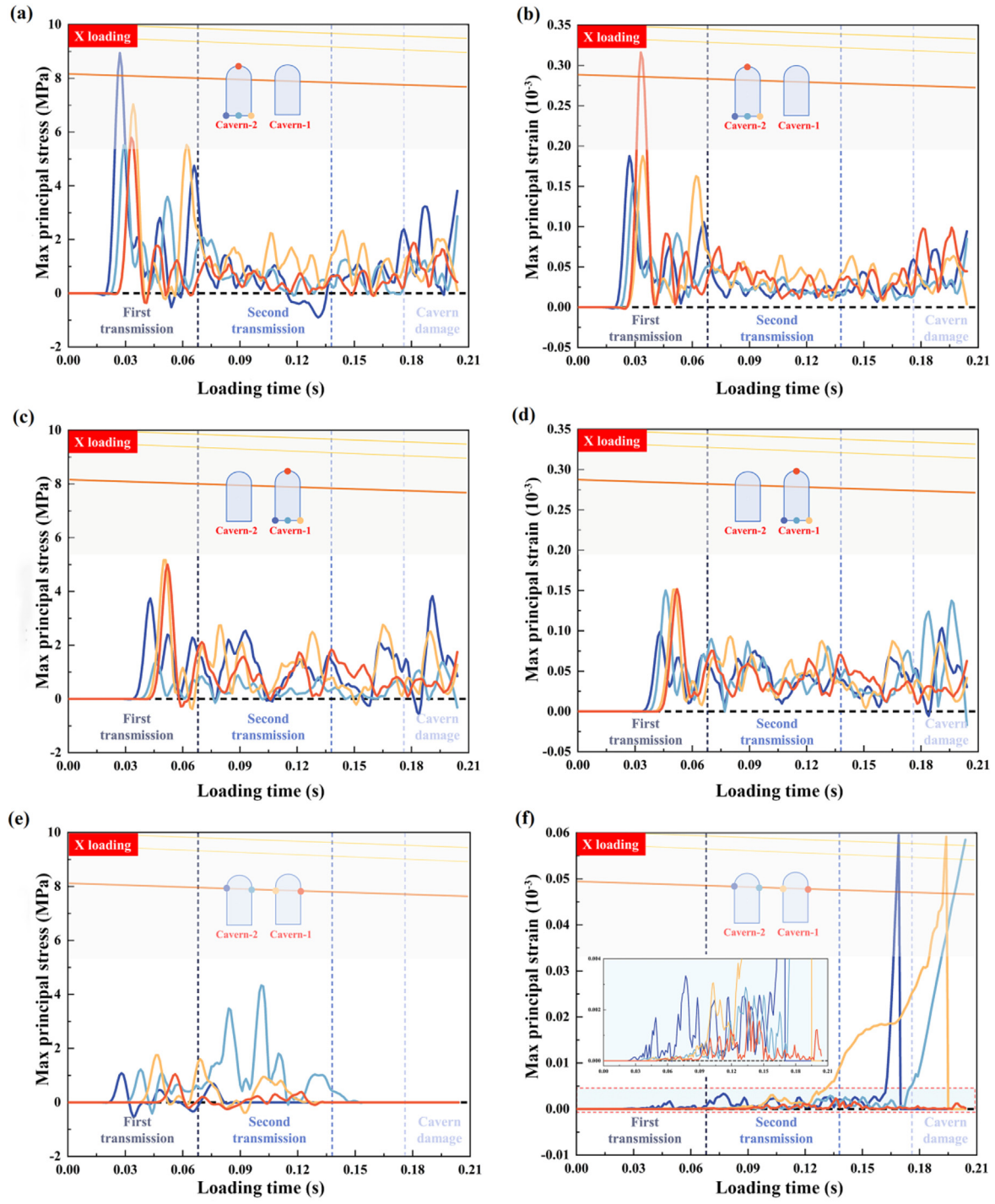

Fig. 12. Stress and strain time history curves of different cavern positions under dynamic loading along the *X*-direction.

parallel to the interlayer joints and ISWZs and then penetrate the entire model. Additionally, the ISWZ significantly adjusts the stress concentration in the cavern. When the ISWZ passes through the cavern, the internal stress of the cavern shifts from the tensile stress of the single cavern to the upper compressive and lower tensile stresses in the double cavern, showing a significant discontinuity. Thus, under *Y*-direction loading, an increase in the number of caverns can still adjust compressive stress, exacerbating the damage at the interlayer joints and ISWZs.

Stress and strain time history curves were plotted for the interface between the cavern and the ISWZ, as shown in Fig. 20. Similar to the *X*-direction loading, during the dynamic failure process, the rock mass at the interface undergoes strain accumulation, ultimately resulting in brittle failure. In the stress time history curve (Fig. 20a), an increase in the number of caverns significantly reduces early-stage stress peaks but leads to an earlier increase in later-stage stress. The strain increases with the number of caverns, and brittle failure in the rock mass occurs earlier compared to *X*-direction loading. This indicates a negative correlation between the number of caverns and the time to failure of the

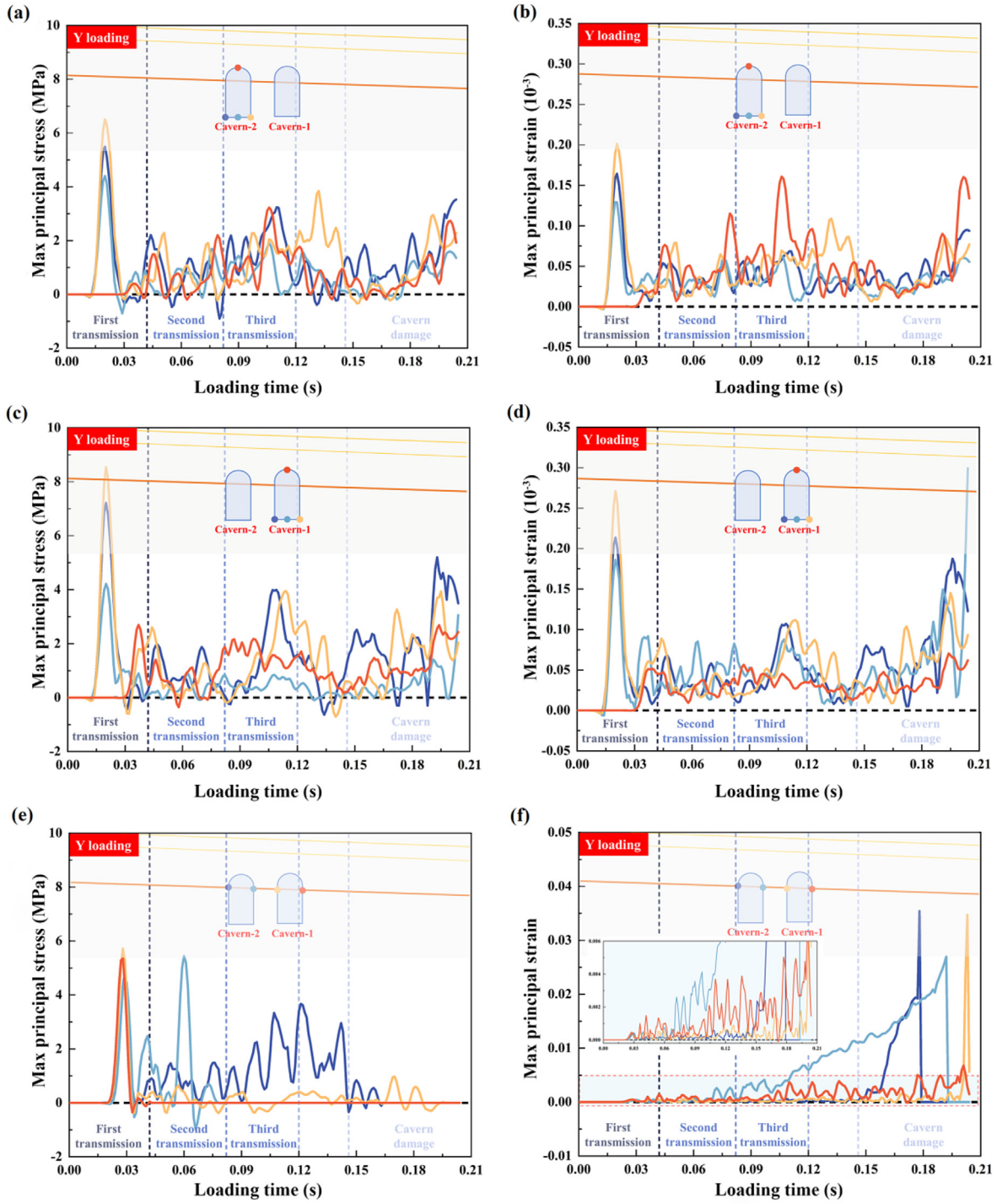

Fig. 13. Stress and strain time history curves of different cavern positions under dynamic loading along the *Y*-direction.

ISWZ under *Y*-direction loading: the more caverns present, the earlier failure occurs. Additionally, the presence of caverns suppresses early-stage stress fluctuations during loading, further influencing the dynamic response of the ISWZ.

Fig. 21 shows the horizontal stress and strain distribution curves at the top and bottom of the cavern after the third stress propagation ($t = 0.124$ s). From the bottom stress curve (Fig. 21a), it can be observed that the presence of a single cavern increases the area and magnitude of tensile stress distribution. The stress peaks are located on both sides of the cavern but remain below the stress limit. In contrast, the presence of a double cavern reduces both the stress peaks and the magnitude of the tensile stress. The horizontal strain curve follows a similar pattern and the existence of caverns can adjust the location of strain peaks. The double cavern structure significantly reduces the strain peaks produced by a single cavern. Due to its location in the CJRMs, the cavern top experiences severe stress fluctuations (Fig. 21c). The cavern top, due to its special structural location, exhibits complex strain changes (Fig. 21d). The

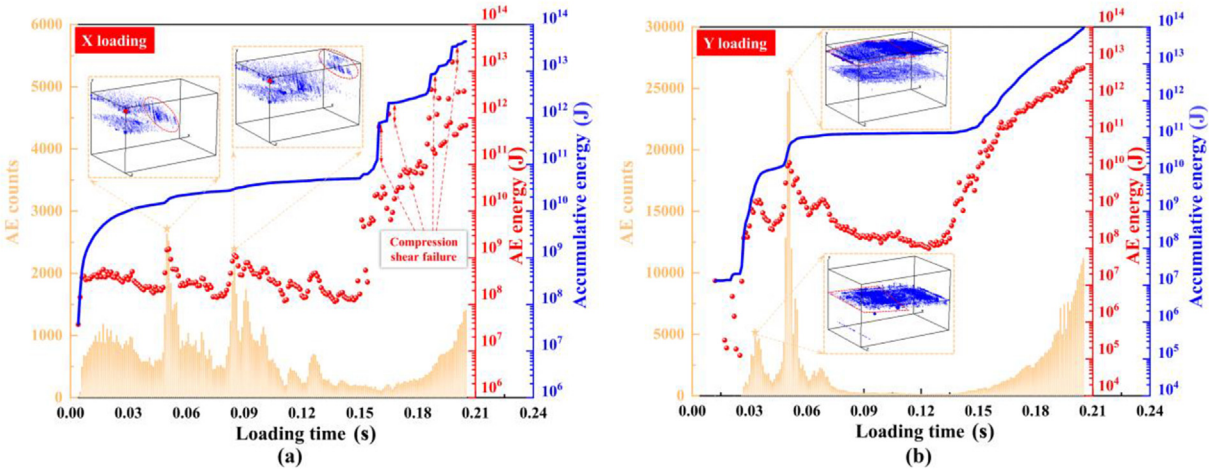

Fig. 14. Variation curves of AE count and energy with time under dynamic loading in different directions: (a) Loading along the *X*-direction; and (b) Loading along the *Y*-direction.

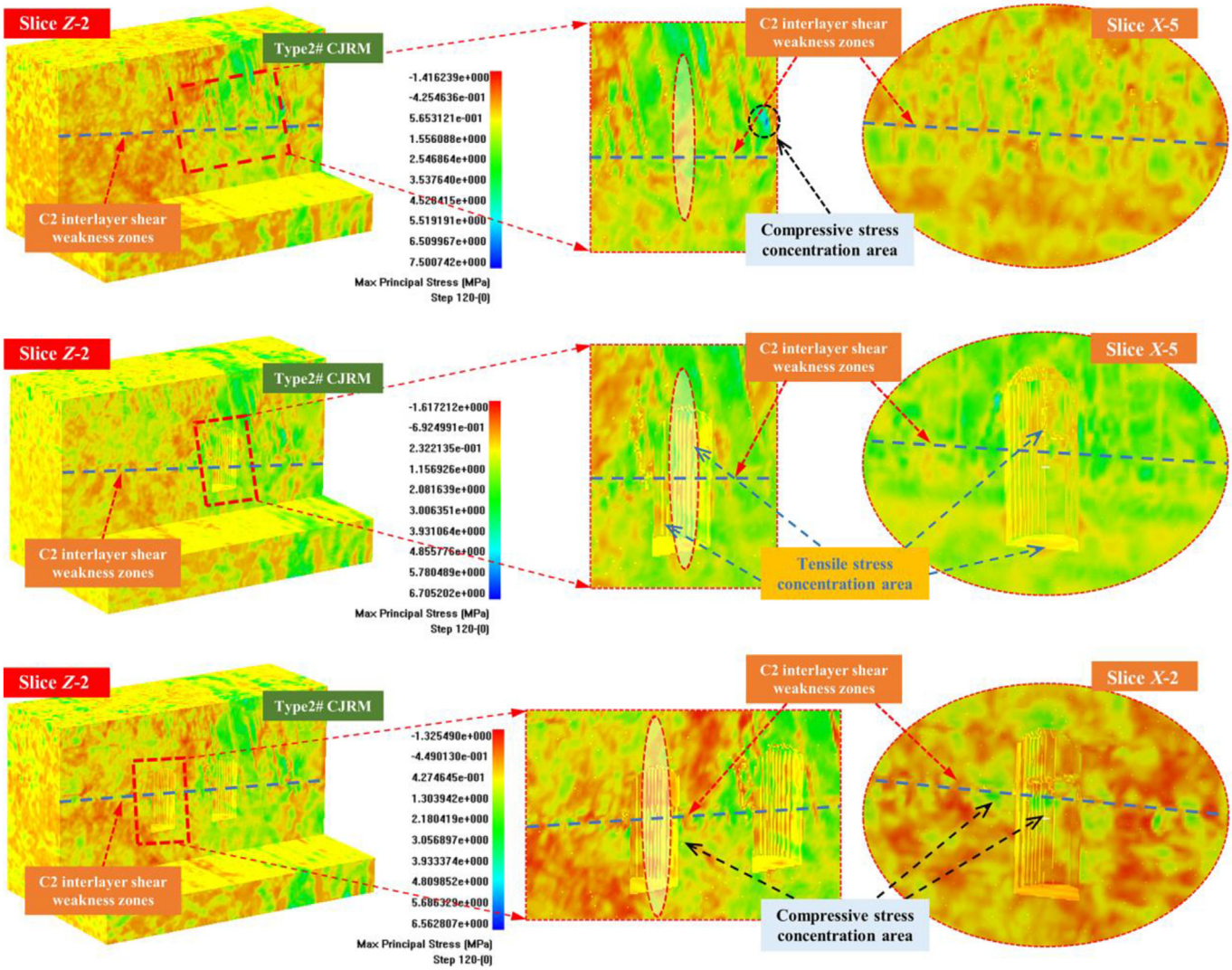

Fig. 15. Failure modes and maximum principal stress cloud diagrams of different numbers of caverns under dynamic loading along the *X*-direction.

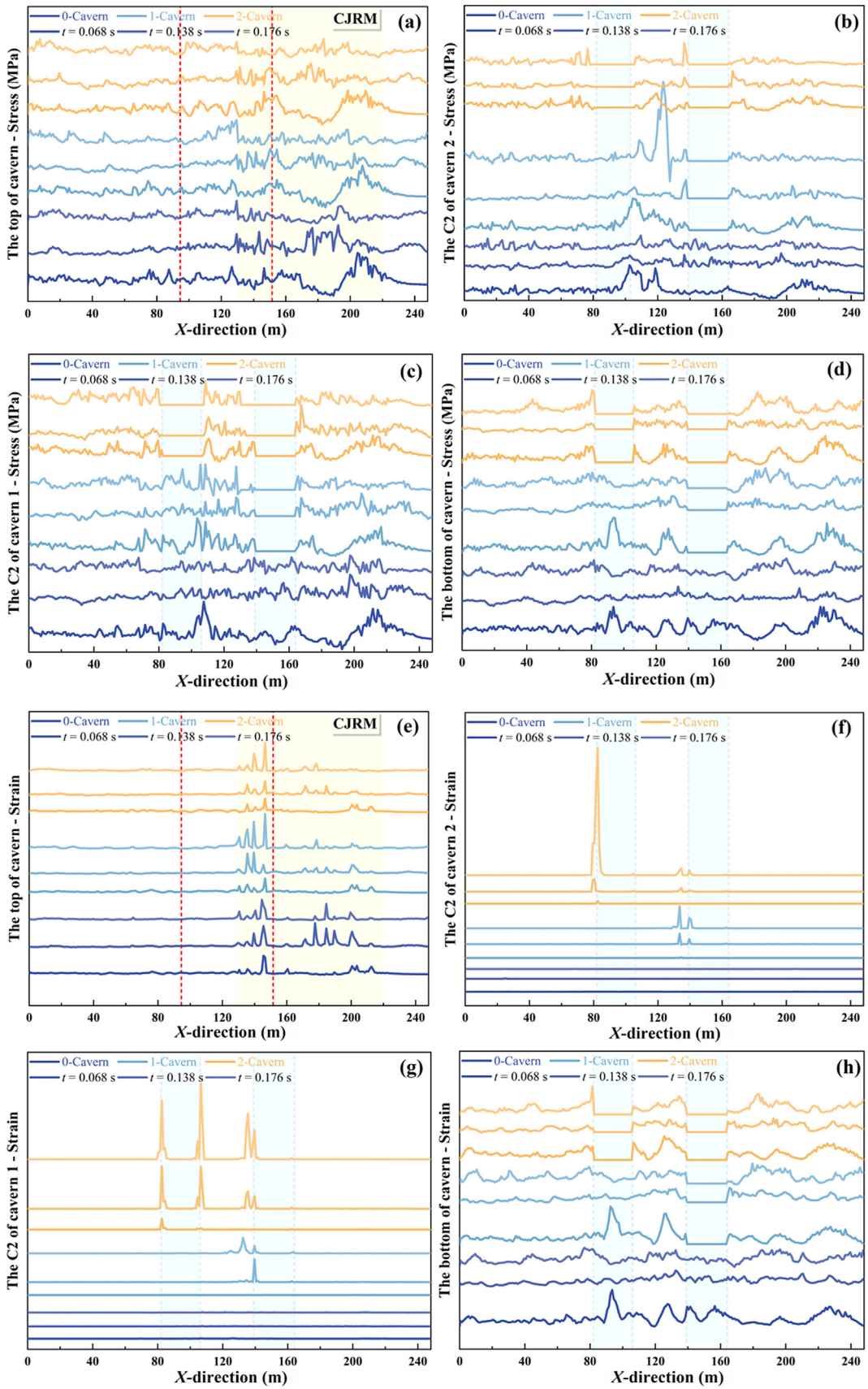

Fig. 16. Horizontal stress and strain distribution curves of weak structures in the cavern at different stress propagation stages under dynamic loading along the *X*-direction: (a)–(d) Horizontal stress distribution; and (e)–(h) Horizontal strain distribution.

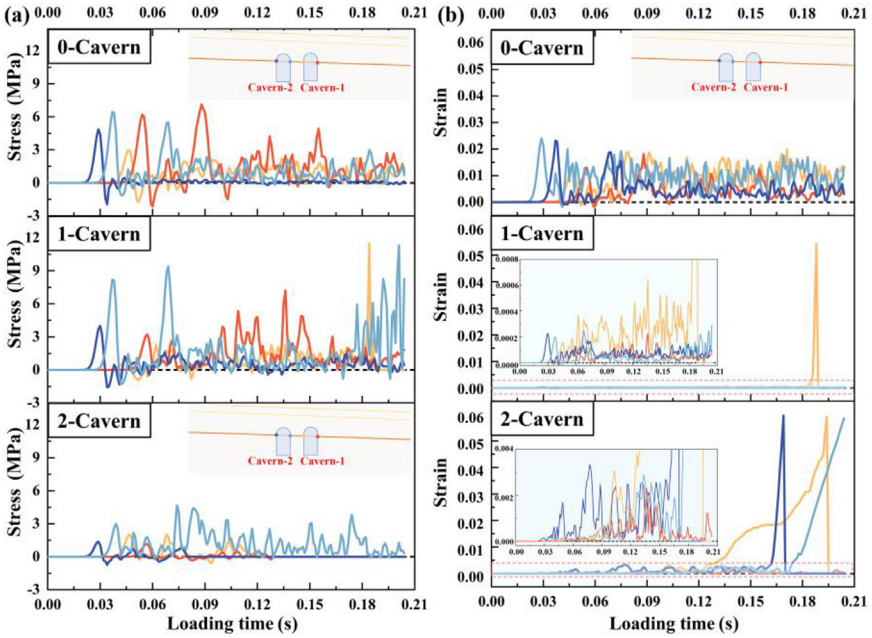

Fig. 17. Stress and strain time-history curves at the interface between the ISWZ and cavern under dynamic loading along the *X*-direction: (a) Stress time-history curve; and (b) Strain time-history curve.

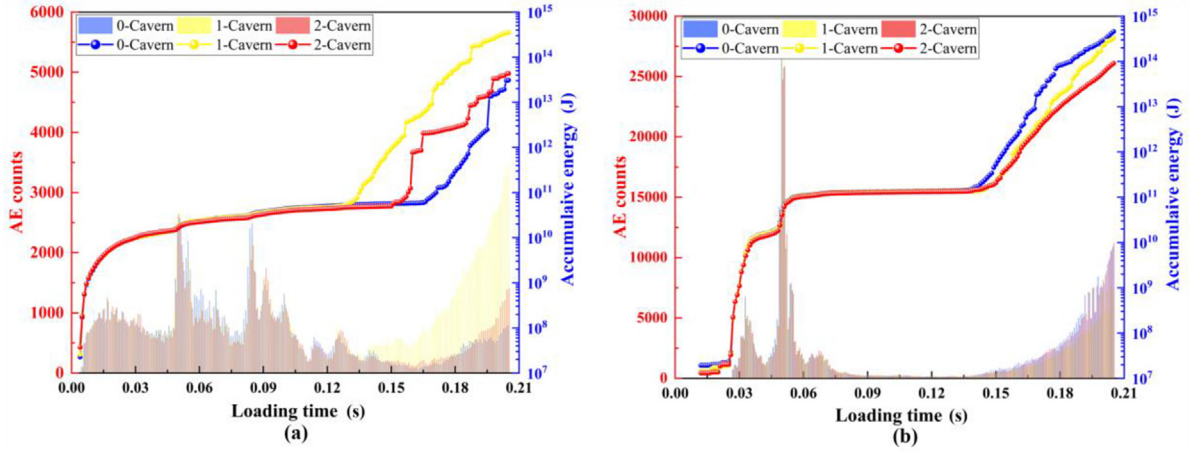

Fig. 18. The AE count and energy curves with different numbers of caverns under dynamic loading in different directions: (a) Loading along the *X*-direction; and (b) Load along the *Y*-direction.

existence of caverns increases horizontal stress peaks, with intense stress fluctuations. Although stress changes are complex, horizontal strain is relatively minor. The CJRM area experiences severe strain fluctuations. The presence of caverns effectively reduces surrounding strain fluctuations, but due to the lack of support after excavation, large strains occur, especially near the top of the caverns.

Fig. 18b shows the time-varying curves of single-step AE count and accumulative energy under *Y*-direction loading. For the *Y*-direction loading, the presence of caverns does not change the constraint conditions of rock mass in the loading direction. The number of single-step AE counts and energy decreases with an increase in the number of caverns. Meanwhile, the presence of caverns also reduces the compressive stress of the structure. Therefore, under *Y*-direction loading, an increase in the number of caverns can enhance the dynamic stability of the underground cavern structure. The stability of a double cavern structure is better than that of a single cavern, which is better than a structure without a cavern.

4.3. Dynamic response of caverns under different structures

In various weak structures, the causes of cavern structure failure are also complex. Therefore, studying the dynamic stability of different structures in rock engineering is significant. In this model, the CJRM and ISWZ have a significant impact on the stability of the caverns. Thus, we established two other numerical models: one without ISWZ and another without CJRMs, applying the same dynamic loading to them. The stress and damage cloud diagrams of underground caverns with different structures under different direction dynamic loadings are obtained through numerical simulation, as shown in Fig. 22. Under *X*-direction loading when the rock mass is not failing and at the same stress propagation time, the stress distribution within the caverns varies depending on the

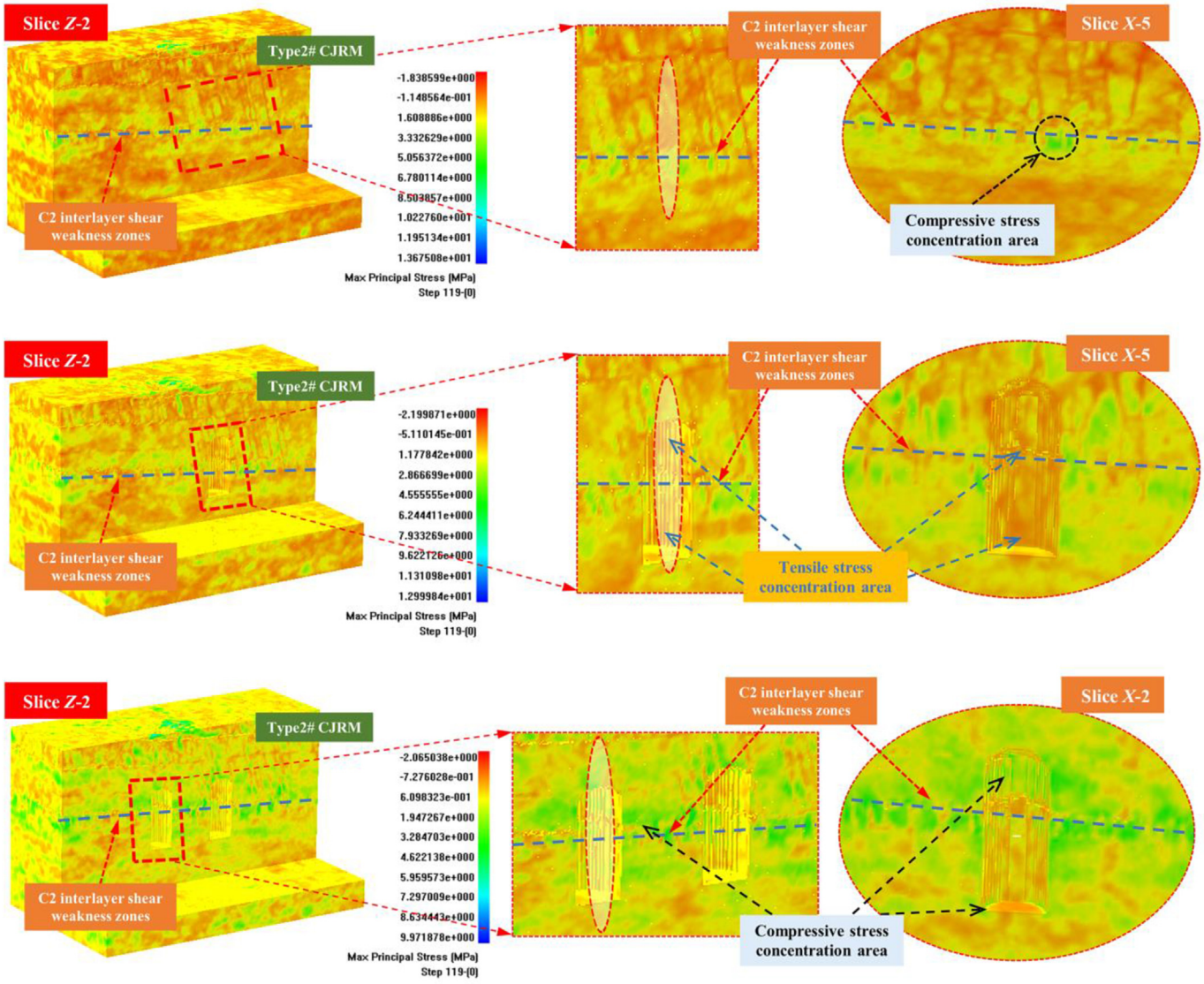

Fig. 19. Failure modes and maximum principal stress cloud diagrams of different numbers of caverns under dynamic loading along the *Y*-direction.

structural configuration. The structure without ISWZ exhibits the highest compressive stress and the lowest tensile stress. In contrast, the structure without CJRMs shows the opposite pattern, with the lowest compressive stress and the highest tensile stress. When the model reaches failure, both the initial rock mass model and the model without ISWZ show failure areas, and their locations are close. Moreover, the model without ISWZ experiences failure earliest. And the structure without CJRMs has the latest failure time. This also shows the primary role of the CJRMs in failure. Furthermore, in the damage cloud diagrams, structural damage is parallel to the distribution of the CJRMs. With the disappearance of the ISWZ structure, there is no significant change in damage and failure areas, but time has advanced. This indicates that the presence of the ISWZ suppresses failure induced by the CJRMs to some extent. In the structure without CJRMs, damaged areas are distributed along the ISWZ and interlayer joints and do not form clear failure faces. Under *Y*-direction loading, the stress cloud diagrams of different structures show the same pattern. The structure without ISWZ has the maximum compressive stress and minimum tensile stress, and the structure without CJRMs has the minimum compressive stress and maximum tensile stress. Additionally, comparing the three structures, it can be noted that in the initial structure and the structure without CJRMs, there are three horizontal cracks. However, in the absence of ISWZ, there are only two. Furthermore, in the damage cloud diagrams, both the initial structure and the structure without ISWZ show areas of destruction. The difference is that the initial structure has failure areas in the ISWZ and appeared slightly later. It also indicates that the presence of an interlayer shear weakness zone suppresses the failure induced by the CJRMs. The structure without CJRMs only shows three horizontally distributed damage areas, without clear failure. This once again proves the significant role of the CJRMs in failure and their significant impact on the stability of caverns.

Fig. 23 shows the curves of AE count and energy under different direction loadings for caverns with different structures. Under *X*-direction loading (Fig. 23a), the initial structure and the structure without ISWZ generate far more AE counts and energy than the structure without CJRMs. In the early stages of loading, the initial structure, with weak geological structures, has a larger number of AE counts and energy. In the later stages of loading, the structure without ISWZ reaches the failure stage first. Hence, with a rapid increase in the number of AE counts, accumulation energy exceeds

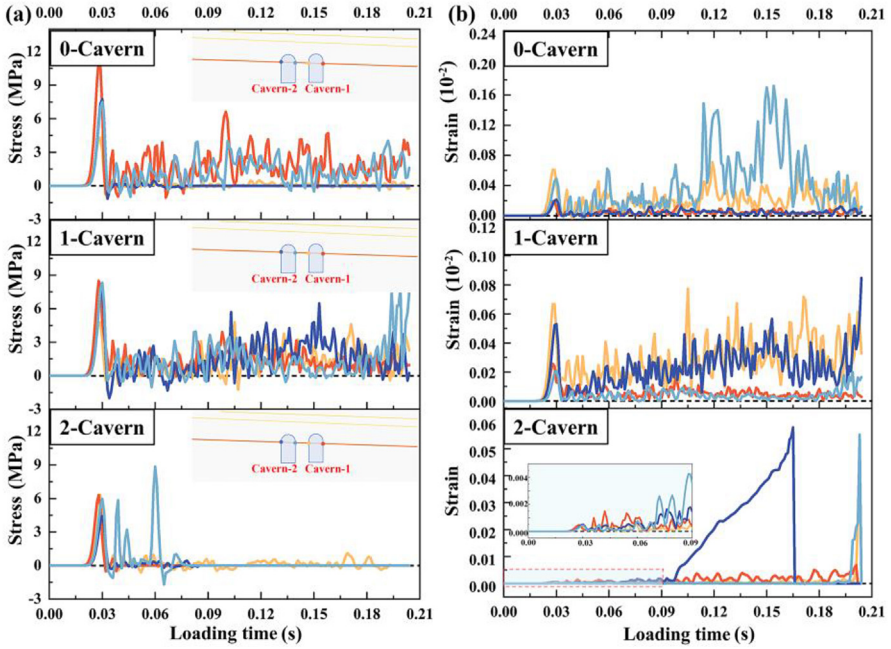

Fig. 20. Stress and strain time-history curves at the interface between the ISWZ and cavern under dynamic loading along the *Y*-direction: (a) Stress time-history curve; and (b) Strain time-history curve.

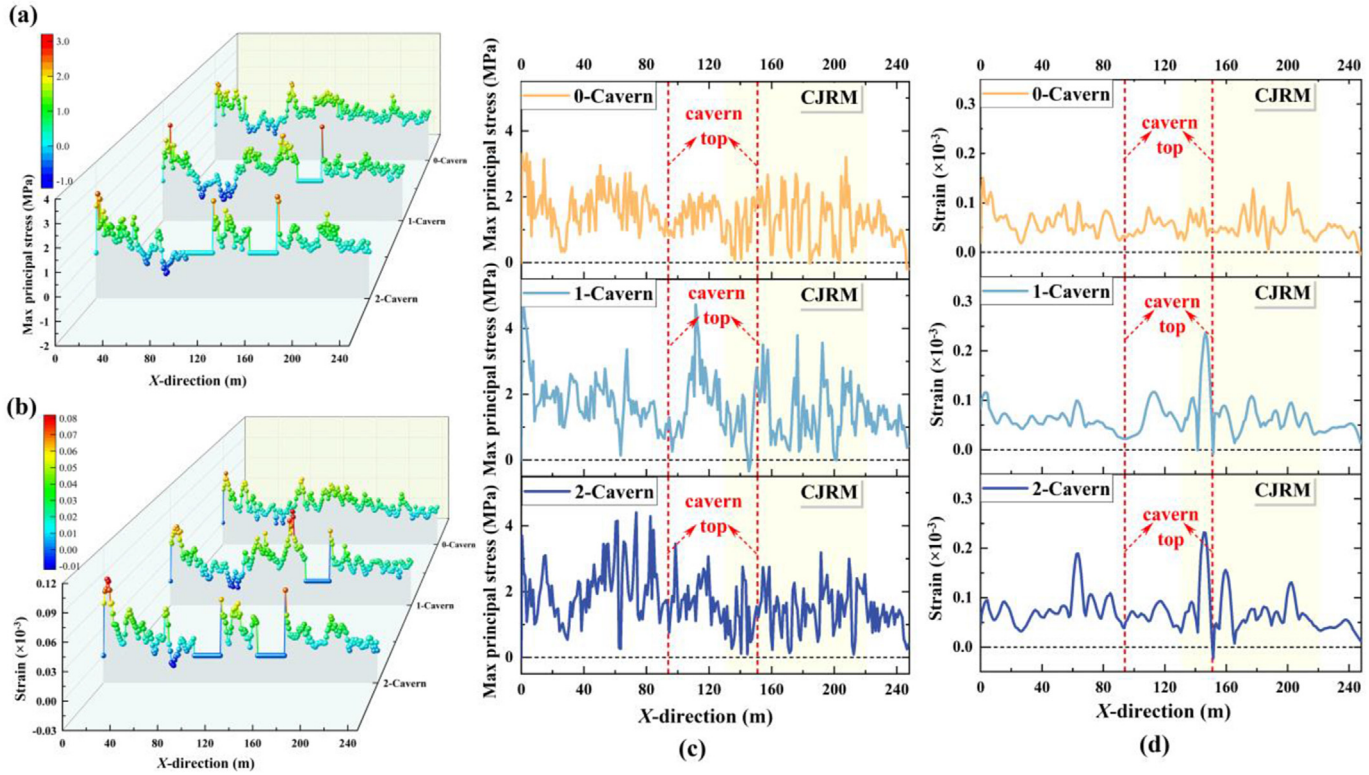

Fig. 21. Horizontal stress and strain distribution curves at the top and bottom of the cavern at $t = 0.124$ s under dynamic loading along the *Y*-direction: (a), (c) Horizontal stress distribution; and (b), (d) Horizontal strain distribution.

the initial structure. The pattern of AE under *Y*-direction loading (Fig. 23b) is consistent with that under *X*-direction loading. The difference is that in the early stages of loading, the structure without CJRMs has more AE counts and energy. This is because the fewer the structures in the *Y*-direction, the faster the stress propagation and the earlier the rock generates AE. However, due to the fewer and fixed number of weak units, it is surpassed. It can be seen that the CJRMs play a significant role in the failure of cavern structures and affect the dynamic stability of caverns.

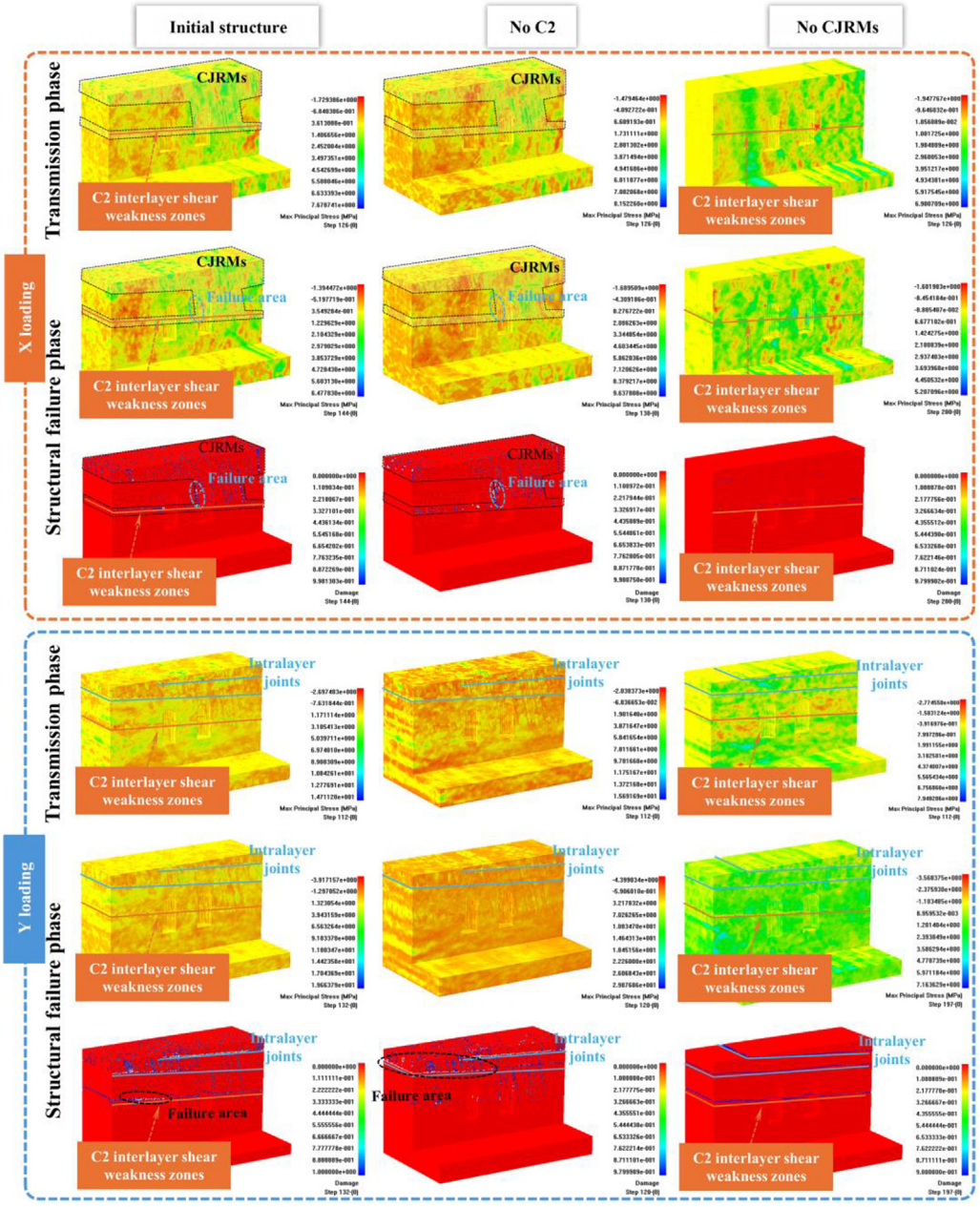

Fig. 22. The maximum principal stress and damage cloud diagram of underground caverns with different weak structures.

5. Discussions

5.1. Dynamic response of multi-number caverns

There are four underground surge caverns on the left bank of Baihetan Hydropower Station. The previous models considered only a double cavern model due to factors such as the number of elements, computation time, and software computational capacity. To further match the number of surge caverns in actual engineering, a model measuring 412 m × 150 m × 75 m, comprising 4,635,000 elements, was established after trial calculations. The dynamic loading scheme considers only *X*-direction loading, with stress wave parameters consistent with previous sections.

Through 3D numerical simulation, the dynamic loading processes of numerical models under different numbers of caverns are obtained. At $t = 0.20$ s, the stress distributions in the central cross-section of the structures are drawn as a stress cloud diagram, as shown in Fig. 24. From the diagram, caverns are sequenced from left to right as Cavern 4, 3, 2, 1. Under dynamic loading, compressive stress concentration areas are primarily distributed around the CJRMs and the bottom of Cavern-1, while tensile stress concentration areas are located around the CJs and the ISWZ. In the single cavern structure, compressive stress concentration areas appear at the top and bottom right of Cavern-1, whereas the right side of the cavern near the ISWZ becomes a tensile stress concentration area. In the double cavern structure, the peak compressive stress is reduced, and a tensile stress concentration area forms between the top of Cavern-2 and Cavern-1. A small amount of compressive stress appears in the upper part of the ISWZ inside Cavern-2. Under the triple cavern structure, compressive stress is further reduced, and the range of tensile stress around the ISWZ near Cavern-1 is expanded. Meanwhile, a small area of tensile stress appears at the

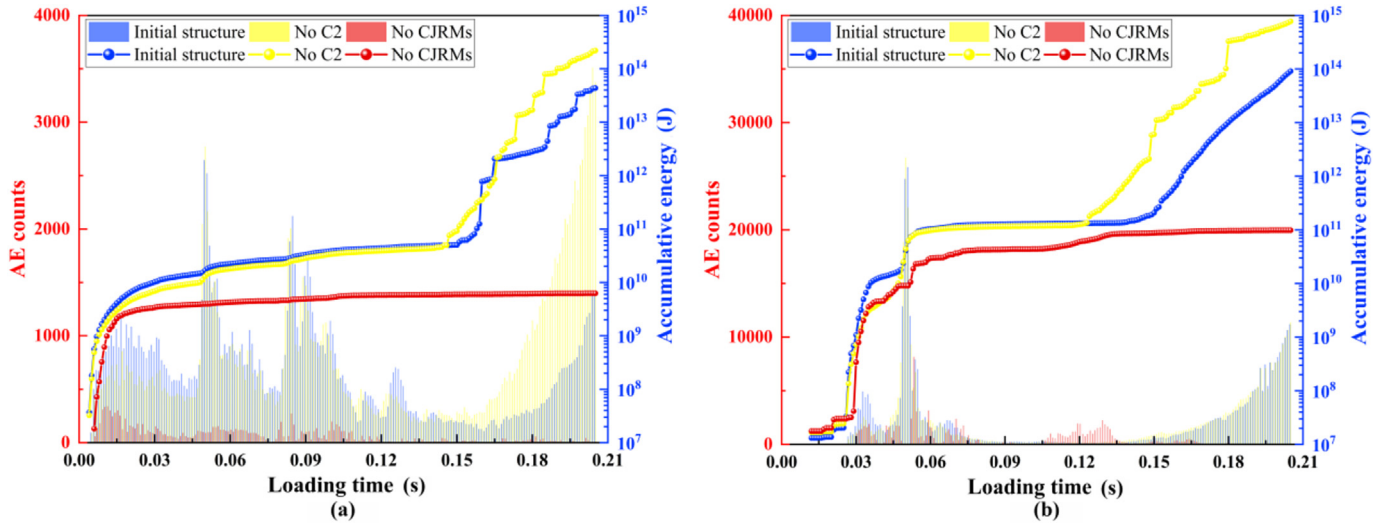

Fig. 23. AE count and energy curves of caverns with different weak structures under loading in different directions: (a) Dynamic loading along the *X*-direction; and (b) Dynamic loading along the *Y*-direction.

top of Cavern-2. Under a quadruple cavern structure, the stress of the whole structure is reduced, and the range of stress distribution is noticeably narrowed. The areas of tensile stress around the ISWZ and the CJRMs are reduced, with obvious cracks in the CJs and ISWZ. From the above analysis, it is clear that an increase in the number of caverns can reduce internal stress in the structure. Additionally, it also can make the whole structure more uniformly stressed and enhance stability. At the same time, the interface between the ISWZ and caverns is prone to tensile failure, which requires reinforcement in engineering.

5.2. Comparison of the failure modes under dynamic and static loading

The failure modes of CJRMs are different under different loading modes. Zhao et al. (2022a) established the large-scale CJRMs numerical model containing ISWZs based on numerical simulation software and carried out triaxial compression simulation under different directions of loading. The simulation results showed that the failure modes of the numerical model of the cavern mainly include compressive shear failure along the rock mass with CJs, tensile slip failure along the ISWZs, and compressive shear failure around the cavern. Tensile slip failure predominantly occurred under *X*-direction loading, where the stress distribution within the cavern exhibited significant discontinuity. Under *Y*-direction loading, failure was caused by the combined effects of CJs, interlayer joints, caverns, and C2 ISWZs, leading to the formation of a fracture network.

However, under dynamic loading, the failure modes of the numerical model shifted predominantly to tensile failure, with differences in the failure element distribution depending on the loading direction. For *X*-direction loading, failure elements were distributed parallel to the CJs, and a "delay" phenomenon was observed during stress propagation. In contrast, for *Y*-direction loading, failure elements were distributed parallel to the ISWZs and interlayer joints.

Additionally, under static loading, the failure of the rock mass resulted from the combined effects of CJs, ISWZs, and caverns. Under dynamic loading, the contributions of different structures to rock mass failure varied. Specifically, the CJRMs played a dominant role in the dynamic failure of the cavern model, while the ISWZs exhibited a restraining effect on failure induced by the CJRMs.

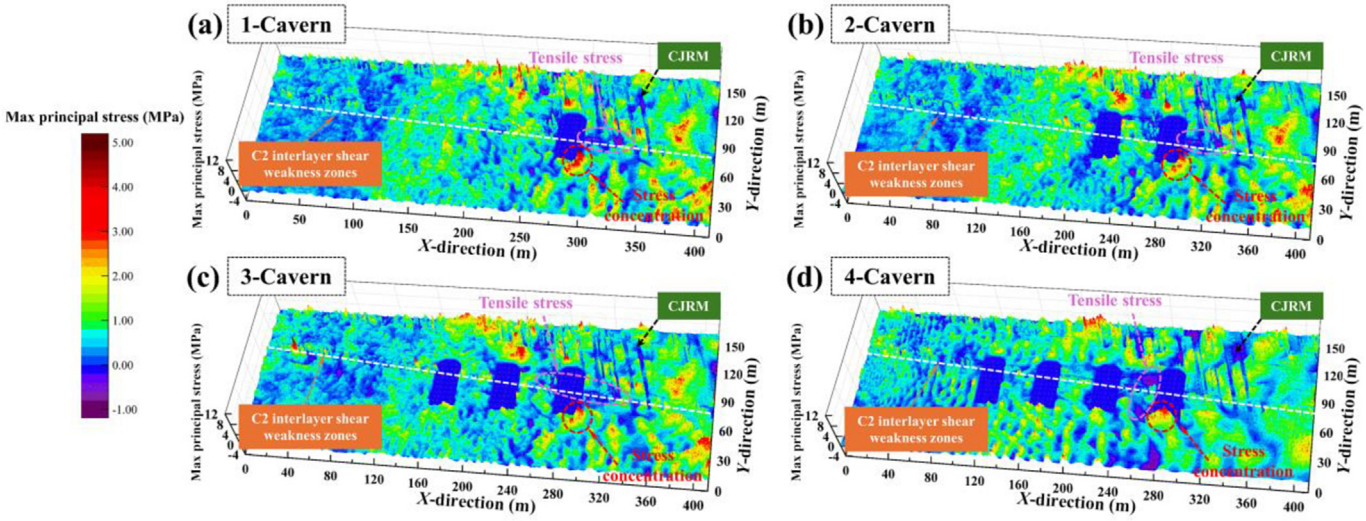

Fig. 24. At $t = 0.20$ s, the maximum principal stress nephogram of the central section of the cavern structure: (a) Single cavern; (b) Double cavern; (c) Three cavern; and (d) Four cavern.

5.3. Limitations and prospects

Investigating the failure modes of large-scale caverns with various complex weak structures is a challenging and time-consuming task, particularly when utilizing physical experiments or numerical simulations. This complexity is especially evident in aspects such as the computational time required for numerical calculations and the calibration of the models. As a result, there are still several issues that need to be addressed in future research, which can be summarized as follows.

(1) Issue 1. The current models do not consider the existence of confining pressure in their boundary conditions.
(2) Issue 2. The dynamic mechanical response of the surrounding rock during the excavation process is overlooked, with studies focusing solely on the excavation of the chamber itself.

In light of these limitations, the authors suggest that future research should emphasize the incorporation of confining pressure, the dynamic mechanical response during excavation, and the development of innovative approaches for calibrating numerical models.

6. Conclusions

In this study, large-scale underground cavern models containing different numbers of caverns and weak structures were established, including ISWZs and CJRMs by the numerical analysis software. By subjecting them to dynamic loading in different directions, the dynamic failure modes, deformation, and AE characteristics of the caverns were analyzed in detail. The main conclusions are as follows.

(1) Under both *X*- and *Y*-direction dynamic loadings, the failure modes of the underground cavern are tensile failures, but their distribution locations differ. Under *X*-direction loading, stress propagation exhibits a significant "delay" phenomenon. The failure mainly occurs parallel to the CJRMs, resulting in vertical cracks within the caverns. Under *Y*-direction loading, no "delay" phenomenon in stress propagation occurs. The failure occurs parallel to horizontal weak structural planes (ISWZs and interlayer joints), leading to horizontal through-cracks parallel to the ISWZs. In both loading directions, rock mass failure occurs at the interface between the ISWZ and the caverns. Additionally, under the same loading time, *Y*-direction loading has more stress propagation instances than *X*-direction loading, making the rock structure more prone to failure.
(2) Under varying numbers of cavern structures, as the number of caverns increases, the internal stress of the overall structure decreases. Damage to weaker areas becomes more pronounced, but early-stage stress and strain fluctuations are significantly suppressed. Additionally, the areas of compressive stress surrounding the caverns decrease, while tensile stress regions expand. Under *X*-direction loading, the double-cavern structure demonstrates the highest stability, whereas the single-cavern structure shows the lowest stability. A similar trend is observed in the number of acoustic emission (AE) counts, with the single-cavern structure recording significantly more AE events than the double-cavern structure. Under *Y*-direction loading, the double-cavern structure again exhibits the best stability, followed by the single-cavern structure, with the structure lacking caverns performing the worst. Notably, AE counts are inversely correlated with the number of caverns.
(3) Among weak structures, the CJRMs play a significant role in structural failure, with the presence of ISWZs suppressing the destruction triggered by the CJRMs. The structure without ISWZ produces the greatest number of AE counts and energy, while the absence of CJRMs results in the least. Additionally, under *X*-direction loading, the area of structural failure is related to the position of dynamic loading and its location, with the side of the cavern closer to the loading position experiencing failure first.

CRediT authorship contribution statement

Yingjie Xia: Supervision, Project administration, Funding acquisition, Conceptualization. **Bingchen Liu:** Writing – original draft, Investigation, Formal analysis. **Danchen Zhao:** Writing – review & editing, Validation, Supervision, Software, Methodology, Data curation. **Chun'an Tang:** Software, Resources. **Hai Yang:** Resources. **Jian Chen:** Resources.

Declaration of competing interest

The authors declare that they have no known competing financial interests or personal relationships that could have appeared to influence the work reported in this paper.

Acknowledgments

This study was funded by the National Natural Science Foundation of China (Grant Nos. 42077251, 41807269, and U1865203).

List of symbols

α	Mechanical parameter of the element
α_0	Scale factor of the average mechanical parameter of the unit
m	Uniformity of rock material
D	Damage variable
E, E_0	Elastic modulus of the material at the current and initial stages
λ	Element residual strength coefficient
$\varepsilon, \varepsilon_{t0}, \varepsilon_{tu}$	Equivalent strain, elastic tensile strain, and ultimate tensile strain
$\varepsilon_1, \varepsilon_2, \varepsilon_3$	Three principal strains of the unit
$\overline{\varepsilon}$	Equivalent strain
σ_1	Maximum principal stress
σ_3	Minimum principal stress
σ_c	Uniaxial compressive strength of the unit
φ	Internal friction angle
$\ddot{u}$, $\dot{u}$, u	Displacement, velocity and acceleration
M, C, K	Mass, damping and stiffness matrices of the system
$\dot{\alpha}_{t+\Delta t}$	Velocity
$\alpha_{t+\Delta t}$	Displacement
β, γ	Integral coefficients of Newmark method

References

Ahmed, M., Iskander, M., 2012. Evaluation of tunnel face stability by transparent soil models. Tunn. Undergr. Space Technol. 27, 101–110.
Aydin, A., 2009. ISRM Suggested method for determination of the Schmidt hammer rebound hardness: revised version. Int. J. Rock Mech. Min. Sci. 46, 627–634.
Aydan, O., Ohta, Y., Genis, M., Tokashiki, N., Ohkubo, K., 2010. Response and stability of underground structures in rock mass during earthquakes. Rock Mech. Rock Eng. 43, 857–875.

Bhasin, R., Hoeg, K., 1998. Parametric study for a large cavern in jointed rock using a distinct element model (UDEC-BB). Int. J. Rock Mech. Min. Sci. Geomech. Abstr. 35, 17–29.
Bosshard, S.A., Mattsson, H.B., Hetényi, G., 2012. Origin of internal flow structures in columnar-jointed basalt from Hrepphólar, Iceland: I. Textural and geochemical characterization. Bull. Volcanol. 74, 1645–1666.
Cai, W., Zhu, H., Liang, W., Vu, B., Wu, W., 2023. Physical and numerical investigation on nonlinear mechanical properties of deep-buried rock tunnel excavation unloading under complicated ground stresses. Tunn. Undergr. Space Technol. 138, 105197.
Cui, Z., Sheng, Q., Leng, X., 2016. Control effect of a large geological discontinuity on the seismic response and stability of underground rock caverns: a case study of the Baihetan #1 surge chamber. Rock Mech. Rock Eng. 49, 2099–2114.
Dai, F., Huang, S., Xia, K., Tan, Z., 2010. Some fundamental issues in dynamic compression and tension tests of rocks using split Hopkinson pressure bar. Rock Mech. Rock Eng. 43, 657–666.
Deng, X.F., Zhu, J.B., Chen, S.G., Zhao, Z.Y., Zhou, Y.X., Zhao, J., 2014. Numerical study on tunnel damage subject to blast-induced shock wave in jointed rock masses. Tunn. Undergr. Space Technol. 43, 88–100.
Deng, X.F., Chen, S.G., Zhu, J.B., Zhou, Y.X., Zhao, Z.Y., Zhao, J., 2015. UDEC–AUTODYN hybrid modeling of a large-scale underground explosion test. Rock Mech. Rock Eng. 48, 737–747.
Fan, Q., Wang, Z., Xu, J., Zhou, M., Jiang, Q., Li, G., 2018. Study on deformation and control measures of columnar jointed basalt for baihetan super-high arch dam foundation. Rock Mech. Rock Eng. 51, 2569–2595.
Feng, X., Hao, X., Jiang, Q., Li, S., Hudson, J.A., 2016. Rock cracking indices for improved tunnel support design: a case study for columnar jointed rock masses. Rock Mech. Rock Eng. 49, 2115–2130.
Fu, X., Sheng, Q., Zhang, Y., Chen, J., 2017. Time-frequency analysis of seismic wave propagation across a rock mass using the discontinuous deformation analysis method. Int. J. GeoMech. 17 (8). https://doi.org/10.1061/(ASCE)GM.1943-5622.0000892.
GB 18306–2015, 2015. Seismic Ground Motion Parameters Zonation Map of China. SAC/TC 225, China.
Guo, H., Sun, Q., Feng, G., Li, S., Xiao, Y., 2023. In-situ observations of damage-fracture evolution in surrounding rock upon unloading in 2400-m-deep tunnels. Int. J. Min. Sci. Technol. 33, 437–446.
Hatzor, Y.H., Feng, X., Li, S., Yagoda-Biran, G., Jiang, Q., Hu, L., 2015. Tunnel reinforcement in columnar jointed basalts: the role of rock mass anisotropy. Tunn. Undergr. Space Technol. 46, 1–11.
Huang, L., 2011. Development and new achievements of rock dynamics in China. Rock Soil Mech. 32, 2889–2900.
Huang, J., Liu, X., Song, D., Zhao, J., Wang, E., Zhang, J., 2022. Laboratory-scale investigation of response characteristics of liquid-filled rock joints with different joint inclinations under dynamic loading. J. Rock Mech. Geotech. Eng. 14, 396–406.
Ishida, T., Kanagawa, T., Uchita, Y., 2014. Acoustic emission induced by progressive excavation of an underground powerhouse. Int. J. Rock Mech. Min. Sci. 71, 362–368.
Ji, H., Zhang, J.C., Xu, W.Y., Wang, R.B., Wang, H.L., Yan, L., Lin, Z.N., 2017. Experimental investigation of the anisotropic mechanical properties of a columnar jointed rock mass: observations from laboratory-based physical modelling. Rock Mech. Rock Eng. 50, 1919–1931.
Jiang, Q., Feng, X., Hatzor, Y.H., Hao, X., Li, S., 2014. Mechanical anisotropy of columnar jointed basalts: an example from the Baihetan hydropower station, China. Eng. Geol. 175, 35–45.
Jiang, Q., Feng, X., Fan, Y., Fan, Q., Liu, G., Pei, S., Duan, S., 2017. In situ experimental investigation of basalt spalling in a large underground powerhouse cavern. Tunn. Undergr. Space Technol. 68, 82–94.
Jiang, Q., Su, G., Feng, X., Chen, G., Zhang, M., Liu, C., 2019. Excavation optimization and stability analysis for large underground caverns under high geostress: a case study of the Chinese Laxiwa project. Rock Mech. Rock Eng. 52, 895–915.
Jiang, Q., Song, L., Yan, F., Liu, C., Yang, B., Xiong, J., 2020a. Experimental investigation of anisotropic wear damage for natural joints under direct shearing test. Int. J. GeoMech. 20 (4). https://doi.org/10.1061/(ASCE)GM.1943-5622.000161.
Jiang, Q., Yang, B., Yan, F., Liu, C., Shi, Y., Li, L., 2020b. New method for characterizing the shear damage of natural rock joint based on 3D engraving and 3D scanning. Int. J. GeoMech. 20 (2). https://doi.org/10.1061/(ASCE)GM.1943-5622.000157.
Jiang, Q., Zhong, S., Pan, P., Shi, Y., Guo, H., Kou, Y., 2020c. Observe the temporal evolution of deep tunnel's 3D deformation by 3D laser scanning in the Jinchuan No. 2 Mine. Tunn. Undergr. Space Technol. 97, 103237.
Jin, C., Yang, C., Fang, D., Xu, S., 2015. Study on the failure mechanism of basalts with columnar joints in the unloading process on the basis of an experimental cavity. Rock Mech. Rock Eng. 48, 1275–1288.
Kwon, S., Lee, C.S., Cho, S.J., Jeon, S.W., Cho, W.J., 2009. An investigation of the excavation damaged zone at the KAERI underground research tunnel. Tunn. Undergr. Space Technol. 24, 1–13.
Li, J.C., Ma, G.W., 2009. Experimental study of stress wave propagation across a filled rock joint. Int. J. Rock Mech. Min. Sci. 46, 471–478.
Li, Y., Zhu, Z., Li, B., Deng, J., Xie, H., 2011. Study on the transmission and reflection of stress waves across joints. Int. J. Rock Mech. Min. Sci. 48, 364–371.
Li, X., Cao, W., Zhou, Z., Zou, Y., 2014. Influence of stress path on excavation unloading response. Tunn. Undergr. Space Technol. 42, 237–246.
Li, G., Tang, C., Liang, Z., 2017. Development of a parallel FE simulator for modeling the whole trans-scale failure process of rock from meso- to engineering-scale. Comput. Geotech.-UK 98, 73–86.
Li, A., Liu, Y., Dai, F., Liu, K., Wei, M., 2020. Continuum analysis of the structurally controlled displacements for large-scale underground caverns in bedded rock masses. Tunn. Undergr. Space Technol. 97, 103288.
Li, A., Dai, F., Liu, Y., Du, H., Jiang, R., 2021. Dynamic stability evaluation of underground cavern sidewalls against flexural toppling considering excavation-induced damage. Tunn. Undergr. Space Technol. 112, 103903.
Liao, Z.Y., Zhu, J.B., Xia, K.W., Tang, C.A., 2016. Determination of dynamic compressive and tensile behavior of rocks from numerical tests of split Hopkinson pressure and tension bars. Rock Mech. Rock Eng. 49, 3917–3934.
Liu, H.Y., Lv, S.R., Zhang, L.M., Yuan, X.P., 2015. A dynamic damage constitutive model for a rock mass with persistent joints. Int. J. Rock Mech. Min. Sci. 75, 132–139.
Liu, Z., Zhang, C., Zhang, C., Wang, H., Zhou, H., Zhou, B., 2022. Effects of amygdale heterogeneity and sample size on the mechanical properties of basalt. J. Rock Mech. Geotech. Eng. 14, 93–107.
Liu, J.S., Zheng, Z.Y., Zhou, H., Zhou, N., Wang, Y., Sun, M.Y., Yang, Y., 2024a. Mechanical characteristic of similar weakly cemented soft rock under directional shear stress path and modified Lade-Duncan, 24 (11), 04024260.
Liu, J.S., Zhu, K.X., Zuo, J.P., Sun, K.Y., Sheng, Y.T., Jia, B.X., 2024b. Soft rock deformation and failure modes under principal stress rotation from roadway excavation. Bull. Eng. Geol. Environ. 83 (8), 355.
Ma, G.L., He, X., Jiang, X., Liu, H.L., Chu, J., Xiao, Y., 2021. Strength and permeability of bentonite-assisted biocemented coarse sand. Can. Geotech. J. 58 (7), 969–981.
Ma, G., He, X., Xiao, Y., Chu, J., Liu, H., Stuedlein, A.W., Evans, T.M., 2024. Spatio-temporal evolution of biomineralization in heterogeneous pore structure. Can. Geotech. J. 61 (3), 447–468.
Manouchehrian, A., Cai, M., 2018. Numerical modeling of rockburst near fault zones in deep tunnels. Tunn. Undergr. Space Technol. 80, 164–180.
Meng, Q., Wang, H., Xu, W., Chen, Y., 2019. Numerical homogenization study on the effects of columnar jointed structure on the mechanical properties of rock mass. Int. J. Rock Mech. Min. Sci. 124.
Mu, W., Li, L., Yang, T., Yu, G., Han, Y., 2019. Numerical investigation on a grouting mechanism with slurry-rock coupling and shear displacement in a single rough fracture. Bull. Eng. Geol. Environ. 78, 6159–6177.
Ning, L., Ping, Z., Duan, Q.W., 2003. Dynamic damage model of the rock mass medium with microjoints. Int. J. Damage Mech. 12, 163–173.
Phillips, J.C., Humphreys, M.C.S., Daniels, K.A., Brown, R.J., Witham, F., 2013. The formation of columnar joints produced by cooling in basalt at Staffa. Scotland. B. Volcanol 75.
Shan, Z., Di, S., 2013. Loading-unloading test analysis of anisotropic columnar jointed basalts. Journal of Zhejiang University. A. Science 14, 603–614.
Shi, A., Wei, Y., Wu, J., Ren, D., Tang, M., 2020. Study on the shear deformation of intralayer shear bands at the Baihetan hydropower station dam foundation. Bull. Eng. Geol. Environ. 79, 3517–3532.
Sun, T., Yue, Z., Gao, B., Li, Q., Zhang, Y., 2011. Model test study on the dynamic response of the portal section of two parallel tunnels in a seismically active area. Tunn. Undergr. Space Technol. 26, 391–397.
Tang, C.A., Tang, S.B., Gong, B., Bai, H.M., 2015. Discontinuous deformation and displacement analysis: from continuous to discontinuous. Sci. China Technol. Sci. 58, 1567–1574.
Tang, C.A., Webb, A.A.G., Moore, W.B., Wang, Y.Y., Ma, T.H., Chen, T.T., 2020. Breaking Earth's shell into a global plate network. Nat. Commun. 11.
Tang, L., Yu, L., Luo, X., Zhou, J., Li, Z., Yang, H., Xiao, Y., 2023. Shaking table test on the seismic response and reinforcement measures of double-arch tunnels in mountainous areas. Tunn. Undergr. Space Technol. 139, 105232.
Wang, T., Huang, T., 2014. Anisotropic deformation of a circular tunnel excavated in a rock mass containing sets of ubiquitous joints: theory analysis and numerical modeling. Rock Mech. Rock Eng. 47, 643–657.
Wang, F., Cao, P., Zhou, C., Li, C., Qiu, J., Liu, Z., 2020. Dynamic compression mechanical behavior and damage model of singly jointed samples. Geomech. Geophys. Geo-Energy Geo-Resour. 6, 71.
Weibull, W., 1951. A statistical distribution function of wide applicability. J. Appl. Mech.-T. ASME 18, 293–297.
Wu, B., Yao, W., Xia, K., 2016. An experimental study of dynamic tensile failure of rocks subjected to hydrostatic confinement. Rock Mech. Rock Eng. 49, 3855–3864.
Xia, Y., Zhang, C., Zhou, H., Chen, J., Gao, Y., Liu, N., Chen, P., 2020a. Structural characteristics of columnar jointed basalt in drainage tunnel of Baihetan hydropower station and its influence on the behavior of P-wave anisotropy. Eng. Geol. 264. https://doi.org/10.1016/j.enggeo.2019.105304.
Xia, Y., Zhang, C., Zhou, H., Hou, J., Su, G., Gao, Y., Liu, N., Singh, H.K., 2020b. Mechanical behavior of structurally reconstructed irregular columnar jointed rock mass using 3D printing. Eng. Geol. 268, 105509.
Xia, Y., Zhang, C., Zhou, H., Shan, Z., Liu, N., Su, G., Gao, Y., Singh, H.K., 2020c. Study on model structure and mechanical anisotropy of columnar jointed rock mass based on three-dimensional printing method. Int. J. GeoMech. 20 (11). https://doi.org/10.1061/(ASCE)GM.1943-5622.0001854.
Xia, Y., Liu, B., Zhang, C., Liu, N., Zhou, H., Chen, J., Tang, C., Gao, Y., Zhao, D., Meng, Q., 2022. Investigations of mechanical and failure properties of 3D printed columnar jointed rock mass under true triaxial compression with one free face. Geomech. Geophys. Geo-Energy Geo-Resour. 8, 26.
Xia, Y., Liu, B., Li, T., Zhao, D., Liu, N., Tang, C.A., Chen, J., 2023. Numerical simulation of failure modes in irregular columnar jointed rock masses under dynamic loading. Mathematics 11, 3790.

Xu, D., Feng, X., Cui, Y., 2012. A simple shear strength model for interlayer shear weakness zone. Eng. Geol. 147–148, 114–123.
Xu, D., Feng, X., Cui, Y., Jiang, Q., 2015. Use of the equivalent continuum approach to model the behavior of a rock mass containing an interlayer shear weakness zone in an underground cavern excavation. Tunn. Undergr. Space Technol. 47, 35–51.
Yang, J., Sheng, Q., Zhu, Z., Leng, X., 2012. Loading/unloading response ratio study of seismic response on underground rock cavern group. Rock Soil Mech. 33, 2127–2132.
Yilmaz, O., Unlu, T., 2013. Three-dimensional numerical rock damage analysis under blasting load. Tunn. Undergr. Space Technol. 38, 266–278.
Zhang, X., Jiao, Y., Ma, J., 2018. Simulation of rock dynamic failure using discontinuous numerical approach. Comput. Geotech. 96, 160–166.
Zhao, D., Xia, Y., Zhang, C., Tang, C., Zhou, H., Liu, N., Singh, H.K., Zhao, Z., Chen, J., Mu, C., 2022a. Failure modes and excavation stability of large-scale columnar jointed rock masses containing interlayer shear weakness zones. Int. J. Rock Mech. Min. Sci. 159, 105222.
Zhao, D., Xia, Y., Zhang, C., Zhou, H., Tang, C.A., Liu, N., Chen, J., Wang, P., Wang, C., 2022b. Laboratory test and numerical simulations for 3D printed irregular columnar jointed rock masses under biaxial compression. Bull. Eng. Geol. Environ. 81.
Zhao, D., Xia, Y., Zhang, C., Liu, N., Tang, C., Singh, H.K., Chen, J., Wang, P., 2023. A new method to investigate the size effect and anisotropy of mechanical properties of columnar jointed rock mass. Rock Mech. Rock Eng. 56, 2829–2859.
Zhu, W.S., Sui, B., Li, X.J., Li, S.C., Wang, W.T., 2008. A methodology for studying the high wall displacement of large-scale underground cavern complexes and it's applications. Tunn. Undergr. Space Technol. 23, 651–664.
Zhu, W.C., Li, Z.H., Zhu, L., Tang, C.A., 2010. Numerical simulation on rockburst of underground opening triggered by dynamic disturbance. Tunn. Undergr. Space Technol. 25, 587–599.
Zhu, W.C., Wei, J., Zhao, J., Niu, L.L., 2014. 2D numerical simulation on excavation damaged zone induced by dynamic stress redistribution. Tunn. Undergr. Space Technol. 43, 315–326.

Danchen Zhao obtained his MSc degree from Dalian University of Technology (Supervisor: Prof. Chun'an Tang and Yingjie Xia) and is currently pursuing a Ph.D. at The Hong Kong Polytechnic University (Supervisor: Prof. Zhenyu Yin). Zhao has published multiple SCI-indexed papers in prestigious journals, including International Journal of Rock Mechanics and Mining Sciences (IJRMMS), Rock Mechanics and Rock Engineering (RMRE), Journal of Rock Mechanics and Geotechnical Engineering (JRMGE), Construction and Building Materials (CBM), and Bulletin of Engineering Geology and the Environment (BOEG). Zhao's research focuses on three-dimensional reconstruction and numerical simulation of complex structural rock masses, development of PD-DEM coupled algorithms, and studies on 3D-printed high-strength, high-brittleness rock-like materials.